Supporting Information

Enhanced Cuprophilic Interactions in Crystalline Catalysts Facilitate the Highly Selective Electroreduction of CO_2 to CH_4

Lei Zhang,[†,⊥] Xiao-Xin Li,[¶,⊥] Zhong-Ling Lang,[#,⊥] Yang Liu,[ʃ] Jiang Liu,[†] Lin Yuan,[†] Wan-Yue Lu,[†] Yuan-Sheng Xia,[†] Long-Zhang Dong,[†] Da-Qiang Yuan[§] and Ya-Qian Lan*[,†,‡]

[†] Jiangsu Collaborative Innovation Centre of Biomedical Functional Materials, Jiangsu Key Laboratory of New Power Batteries, School of Chemistry and Materials Science, Nanjing Normal University, Nanjing 210023, P. R. China.

[‡] School of Chemistry, South China Normal University, Guangzhou, 510006, P. R. China.

[#] Key Laboratory of Polyoxometalate Science of the Ministry of Education, Faculty of Chemistry, Northeast Normal University. Changchun, 130000, P. R. China.

[§] State Key Laboratory of Structural Chemistry Fujian Institute of Research on the Structure of Matter, Chinese Academy of Sciences Fuzhou, 350002, P. R. China.

[¶] School of Chemistry and Chemical Engineering, Southeast University, Nanjing 211189, P. R. China.

[ʃ] Analysis and Testing Center, Tianjin University, Tianjin, 300072 P. R. China

S1. Materials and measurements

All starting materials, reagents and solvents used in experiments were commercially available, high-grade purity materials and used without further purification. Cupric sulfate ($CuSO_4 \cdot 5H_2O$, 99.0%) was purchased from Shanghai Xinbao Fine Chemical Factory. 1,3-bis(5-(pyridinium-2-yl)-1,2,4-triazol-5-yl) benzene (H_2bptb, 97%) was purchased from Jinan Henghua Technology Corporation LTD. Copper(I) Iodide (CuI, 99.5%), Potassium hydroxide (KOH), N,N-dimethylformamide (DMF, 99.5%), N,N-dimethylacetamide (DMA, 99.0%), Methanol (CH_3OH, 99.5%), Triethylamine (Et_3N, 99.0%) were purchased from China National Medicines Corporation LTD. Nafion (5% w/w in water and 1-propanol) was purchased from Alfa Aesar Chemical Corporation LTD.

Analytical techniques

Thermogravimetric analyses (TGA) of the samples were performed on a Perkin–Elmer TG-7 analyzer heated from room temperature to 800 °C in flowing N_2/O_2 with a heating rate of 20 °C/min. Fourier transform infrared spectroscopy (FTIR) were recorded in the range of 4000-400 cm^{-1} on a Mattson Alpha-Centauri spectrometer using the technique of pressed KBr pellets. Powder X-Ray diffraction (PXRD) measurements were recorded ranging from 5 to 50° at room temperature on a D/max 2500 VL/PC diffractometer (Japan) with equipped with graphite mono-chromatized Cu Kα radiation (λ = 1.54060 Å). CO_2 adsorption isotherms were degassed in vacuum at 120 °C for 12 h and then measured by Quantachrome Instruments Autosorb IQ2 at 273 K and 298K. Nuclear magnetic resonance (NMR) were carried out on an AVANCE III HD-500. The X-ray absorption spectra were collected on the beamline BL07A1 in NSRRC. The radiation was monochromatized by a Si (111) double-crystal monochromator. XANES data reduction and analysis were processed by Athena software. X-ray photoelectron spectroscopy (XPS) were measured on an Escalab Xi+. *In situ* Raman was performed on a RENISHAW inVia. A 50× objective lens was used to focus the laser with 532 nm on the sample. Raman spectrometer was calibrated using Si wafer. *In situ* ATR-FTIR spectra were obtained on a Nicolet 6700 FTIR spectrometer with silicon as the prismatic window. A thin layer of gold film was chemically deposited on the surface of the silicon prismatic prior to each experiment.

Single-Crystal X-ray Analyses.

The diffraction data of **NNU-32** and **NNU-33(S)** were collected on Bruker AXS Apex II CCD diffractometer (Mo Kα, λ = 0.71069 Å) at 293 K. **NNU-33(I)** was measured on an SSRF BL17B diffractometer at the National Facility for Protein Science Shanghai at 100 K. All non-hydrogen atoms were refined with anisotropic displacement parameters and hydrogen positions were fixed at calculated positions and refined isotropically. All structures were solved by the intrinsic phasing method with SHELXT[1] and refined with the full-matrix least-squares technique on F^2 by the

SHELXL-2018[2] program package and Olex-2[3] software. The topological analysis of **NNU-33(S)** was performed with TOPOS[4]. CCDC 2025580 (**NNU-32**) and 2025581 (**NNU-33(S)**) contain the supplementary crystallographic data for the paper. These data can be obtained free of charge from The Cambridge Crystallographic Data Centre. The crystallographic data and structure refinement for **NNU-32** and **NNU-33(S)** are summarized in Table S1. The reason for low bond precision on C–C bonds is due to the disordered solvent molecules and weak crystals diffraction (in the crystal data of **NNU-33(H)**).

Electrochemical measurements.

Preparation of cathode electrodes.

5 mg of electrocatalyst was grinded to powered and then dispersed into H_2O (250 uL) and anhydrous ethanol (200 uL) followed by adding 50 uL Nafion, after mixing with assistance of ultrasonication for at least 30 min to achieve a homogeneous ink. 100 uL of the catalyst ink was pipette onto a carbon paper electrode (S = 0.5 cm × 2 cm) with a loading of 1 mg/cm^2. The electrode was then dried at room temperature slowly for the subsequent electrochemical testing experiments.

Catalytic evaluation.

CO_2 electrolysis was performed in a three-channel flow cell composed of a gas-diffusion layer (GDL), an anion exchange membrane (Fumasep, FAA-3-PK-130) and a Pt plate (1 cm^2) anode as shown in **Scheme S1**. The prepared catalyst and gas-diffusion layer, anion exchange membrane and Pt anode were clamped together in order using polytetrafluoroethylene (PTFE) spacers and then fixed with screws. The electrolyte (1.0 M KOH aqueous solution) was then introduced into the chamber between membrane and the cathode as well as the chamber between the anode and membrane. The electrolyte in cathode and anode were circulated by a peristaltic pump (LongerPump, BT100-2J), with the flow rate of 5 mL min^{-1}. The high-purity CO_2 (99.999%) gas was continuously passed through the flow chamber which is behind the gas-diffusion layer and diffuse into the electrolyte present at the catalyst. The gas flow rate was set as 20 sccm via a mass flow controller (AITOLY, MFC300). A saturated Ag/AgCl reference electrode (CHI111) was located in the catholyte stream and positioned ≈1 cm from the cathode was used to measure the cathodic half-cell potential. All potentials were converted to the reversible hydrogen electrode (RHE) in scale according to the following equation: E(*vs* RHE) = E(*vs* Ag / AgCl) + 0.197 V + 0.0591 V × pH.

All the CO_2 reduction experiments were carried out through a CHI 660e electrochemical workstation. Linear sweep voltammetry (LSV) curves were performed to choose the appropriate potential range for the catalysts. The sweeping range was from 0 to -1.0 V (*vs.* RHE) at a scan rate of 50 mV s^{-1} in 1 M KOH solution with CO_2/Ar flowing. The test of electrocatalytic CO_2RR and LSV were presented with 85% *i*R compensation at ambient pressure and temperature. The cell resistances (R) were measured by electrochemical impedance spectroscopy (EIS) and were

displayed in Table S5. Cyclic voltammograms (CV) were tested under the potential window of −0.05 V to −0.05 V (*vs.* Ag/AgCl) in 1 M KOH solution with various scan rates from 10 to 200 mV s^{-1} without *i*R compensation. Before the CV test, the electrolyte was bubbled with Ar for 30 min.

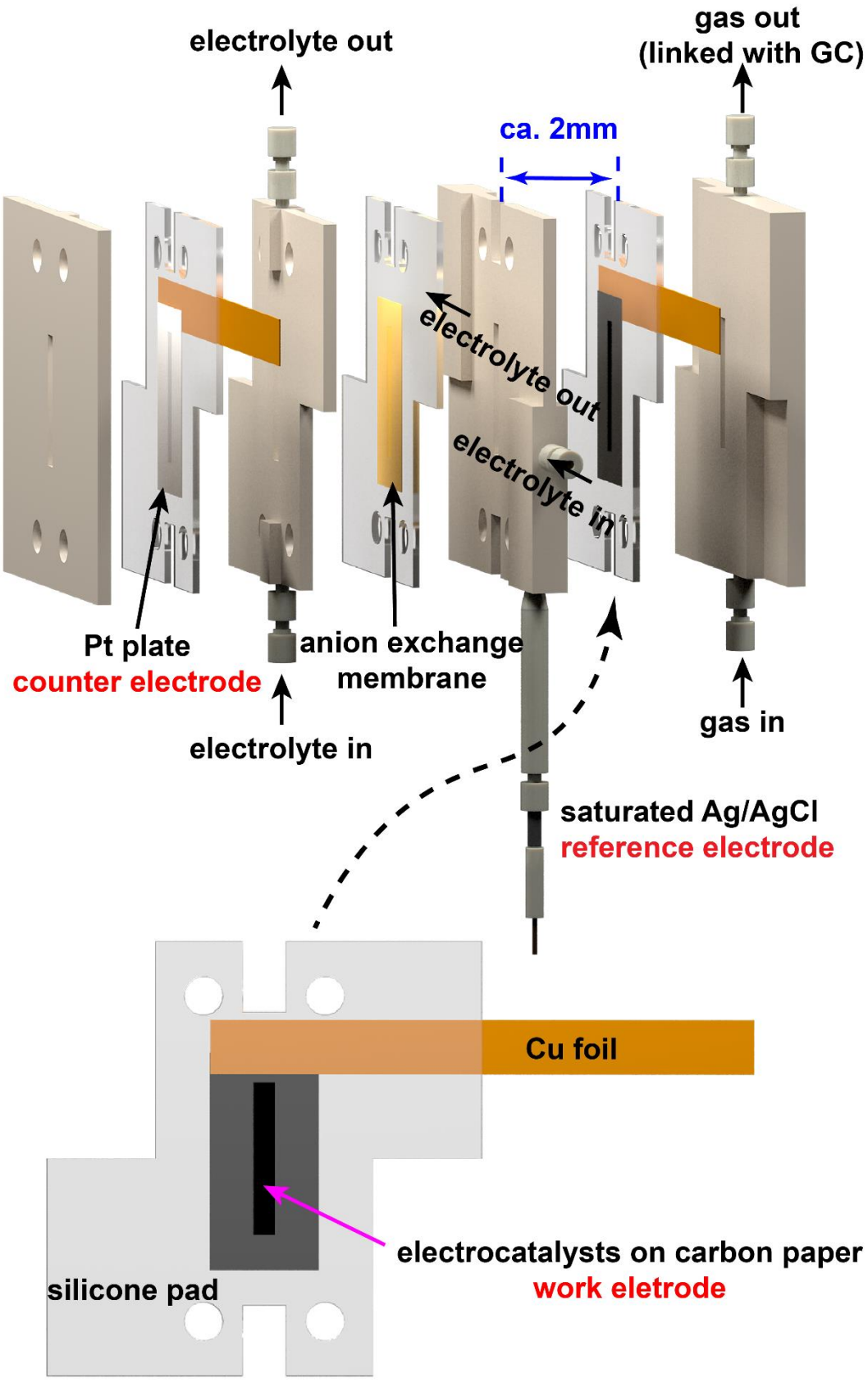

Scheme S1. Diagram of the three-channel flow cell with electrocatalysts deposited on GDE.

Product analysis.

The gas products (H_2, CO, CH_4 and C_2H_4) were analyzed by a gas chromatograph (7820A, Aglient) coupled with a flame ionization detector (FID) and a thermal conductivity detector (TCD) which are equipped with a HP-PLOT Q and Carboxen-1000 columns, respectively. High-purity argon (99.999%) was used as the carrier gas. The outlet of gas in electrolytic cell was directly connected with six-way valve in gas chromatograph through a rubber pipe. The reactions were run for at least 300 s before the gas products were collected for analysis.

The faradaic efficiencies (FEs) were calculated using the following equation:

$$FE\ \% = \frac{nFxV}{j_{Tot}} \times 100$$

Where n = # of electrons transferred

F = Faraday's constant

x = mole fraction of product

V = total molar flow rate of gas

j_{Tot} = total current

The isotope-labeled experiments were performed using $^{13}CO_2$ under almost the same condition as those of $^{12}CO_2$, and the products were analyzed using gas chromatography-mass spectrometry (7890B and 5977B, Aglient) coupled with a GS CARBONPLOT capillary column (Agilent).

The liquid products were analyzed using Nuclear magnetic resonance spectroscopy (NMR). In consideration of the low concentration of liquid products, the 50 mL catholyte was recirculated and collected after 30 min reaction. The ^1H NMR spectra were recorded on an AVANCE III HD-500 in 10 % D_2O water with Dimethyl sulfoxide (DMSO) as an internal standard. $HCOO^-$ was detected to be the only liquid product. In order to analyze the amount of $HCOO^-$ more accurately, an ion chromatography coupled with a SI-52 4E (Shodex) column was utilized. The faradaic efficiencies of $HCOO^-$ were calculated from the results of ion chromatography.

Standard curves on GC.

Four concentrations of standard mixed gases (**1**~**4**) contained H_2, CO, CH_4, C_2H_2, C_2H_4, C_2H_6, C_3H_6 and C_3H_8 with CO_2 balance were used to calculated the standard curves for GC measurements. The concentration of the components (mol/mol) and the final standard curves are listed below.

	H_2	**CO**	**CH_4**	**C_2H_4**
1	0.0000994	0.0000991	0.000101	0.0000995
2	0.0010103	0.0005276	0.000529	0.0005027
3	0.0098212	0.0049362	0.00506	0.0049285
4	0.0497575	0.0204644	0.019919	0.020143

	C_2H_6	C_2H_2	C_3H_6	C_3H_8
1	0.0001018	0.0000999	0.0000982	0.0000992
2	0.0005041	0.0005148	0.000515	0.0005154
3	0.0049414	0.0049138	0.0050022	0.0048827
4	0.0198704	0.019492	0.0198709	0.0197748

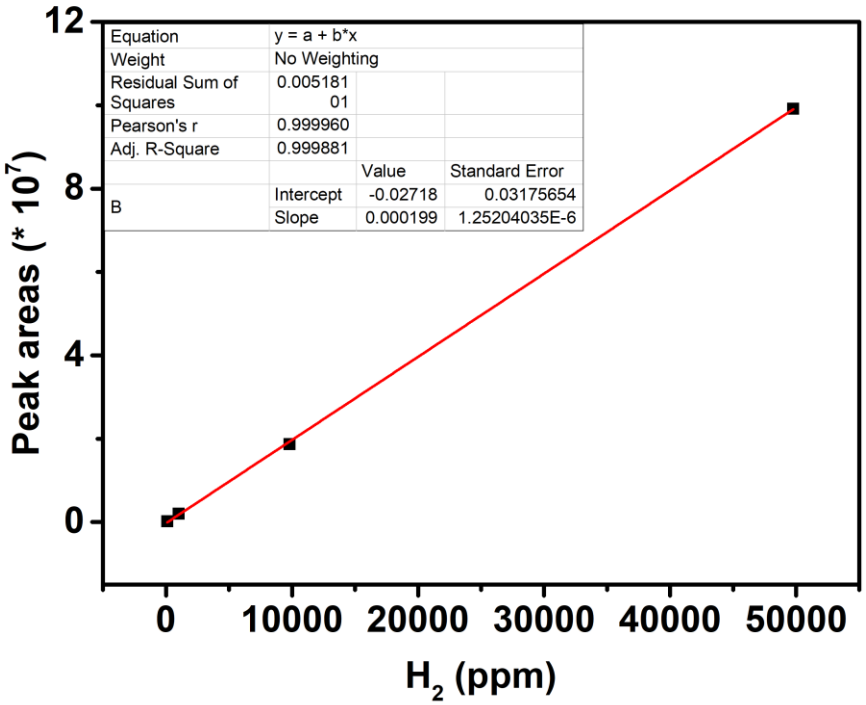

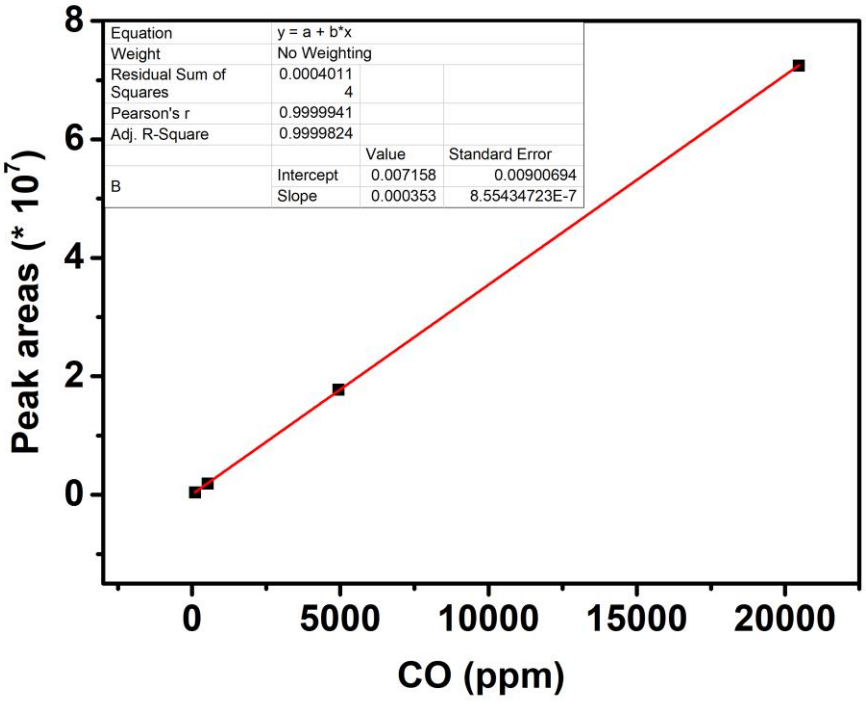

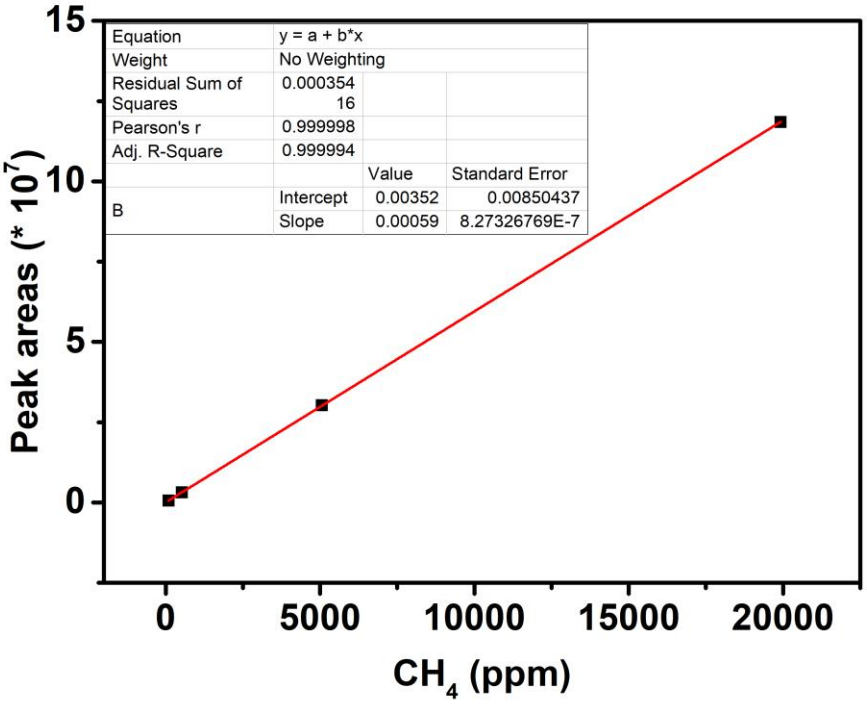
Equation y = a + b*x
Weight No Weighting
Residual Sum of Squares 0.00035416
Pearson's r 0.999998
Adj. R-Square 0.999994
Value Standard Error
B Intercept 0.00352 0.00850437
Slope 0.00059 8.27326769E-7
Peak areas (* 10^7)
CH4 (ppm)
0
5
10
15
0
5000
10000
15000
20000

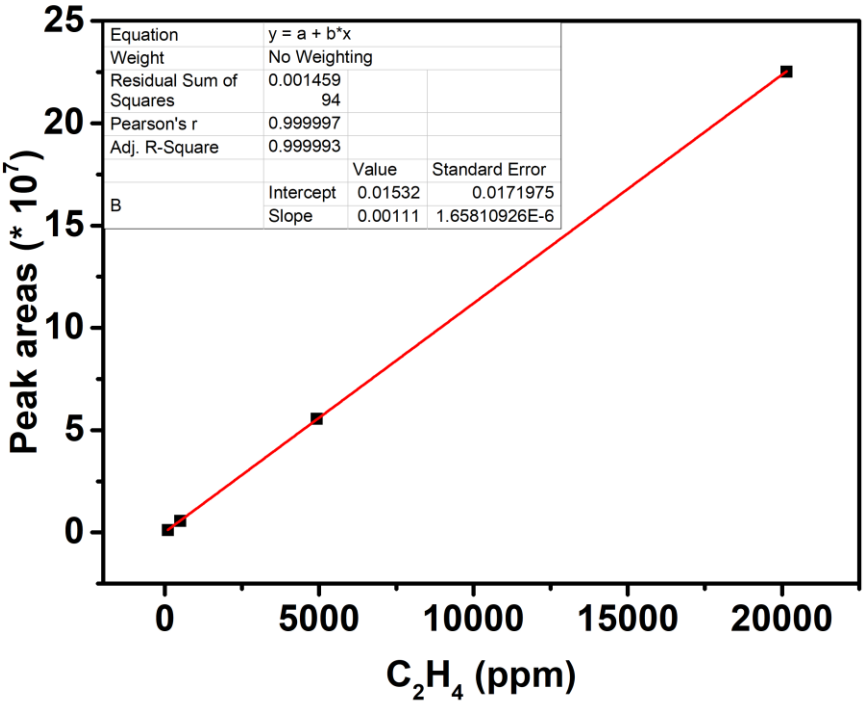
Equation y = a + b*x
Weight No Weighting
Residual Sum of Squares 0.00145994
Pearson's r 0.999997
Adj. R-Square 0.999993
Value Standard Error
B Intercept 0.01532 0.0171975
Slope 0.00111 1.65810926E-6
Peak areas (* 10^7)
C2H4 (ppm)
0
5
10
15
20
25
0
5000
10000
15000
20000

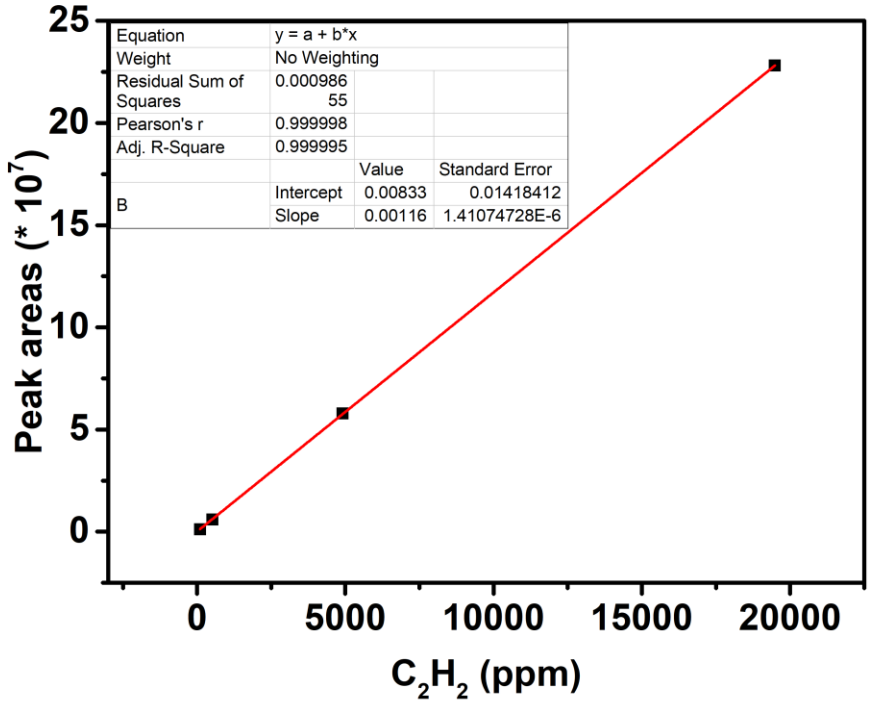
Equation y = a + b*x
Weight No Weighting
Residual Sum of Squares 0.00098655
Pearson's r 0.999998
Adj. R-Square 0.999995
Value Standard Error
B Intercept 0.00833 0.01418412
Slope 0.00116 1.41074728E-6
Peak areas (* 10^7)
C2H2 (ppm)
0
5
10
15
20
25
0
5000
10000
15000
20000

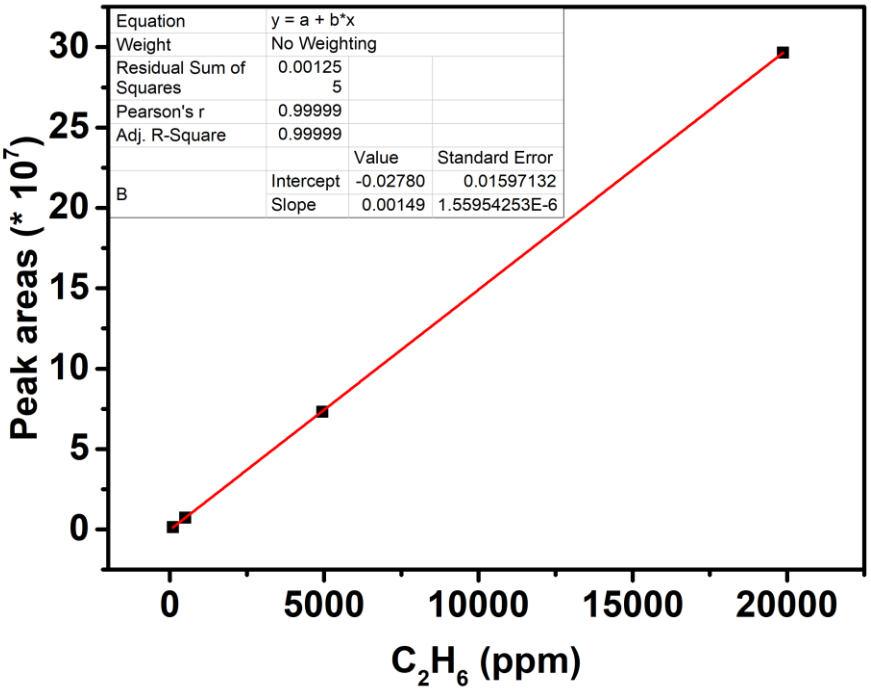
Equation y = a + b*x
Weight No Weighting
Residual Sum of Squares 0.001255
Pearson's r 0.99999
Adj. R-Square 0.99999
Value Standard Error
B Intercept -0.02780 0.01597132
Slope 0.00149 1.55954253E-6
Peak areas (* 10^7)
C2H6 (ppm)
0
5
10
15
20
25
30
0
5000
10000
15000
20000

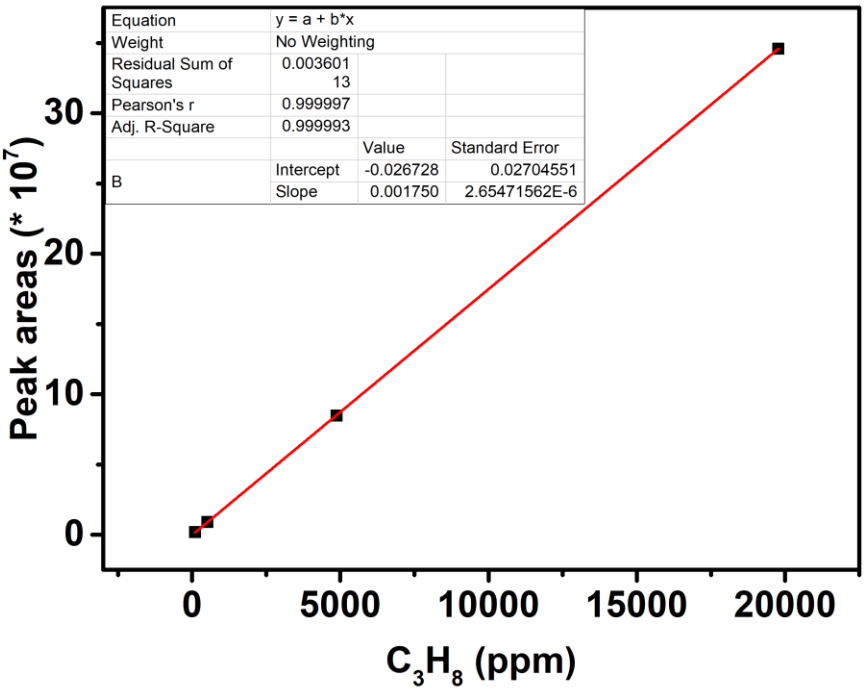

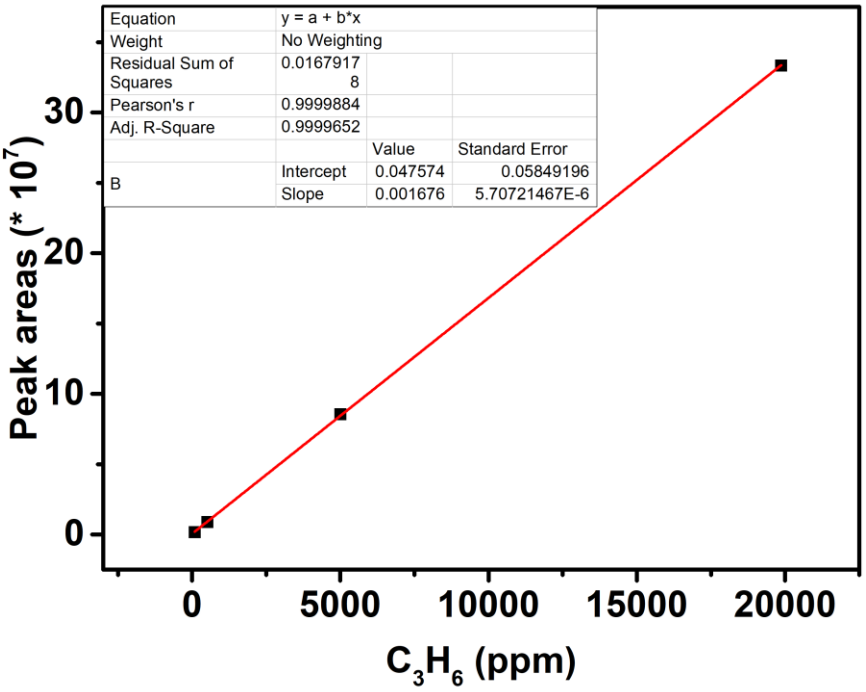

The standard curves of H_2, CO, CH_4, C_2H_4, C_2H_6, C_2H_2, C_3H_6 and C_3H_8. H_2 and CO are detected by TCD and all the hydrocarbons are detected by FID. High linearities ensure the reliability of our data.

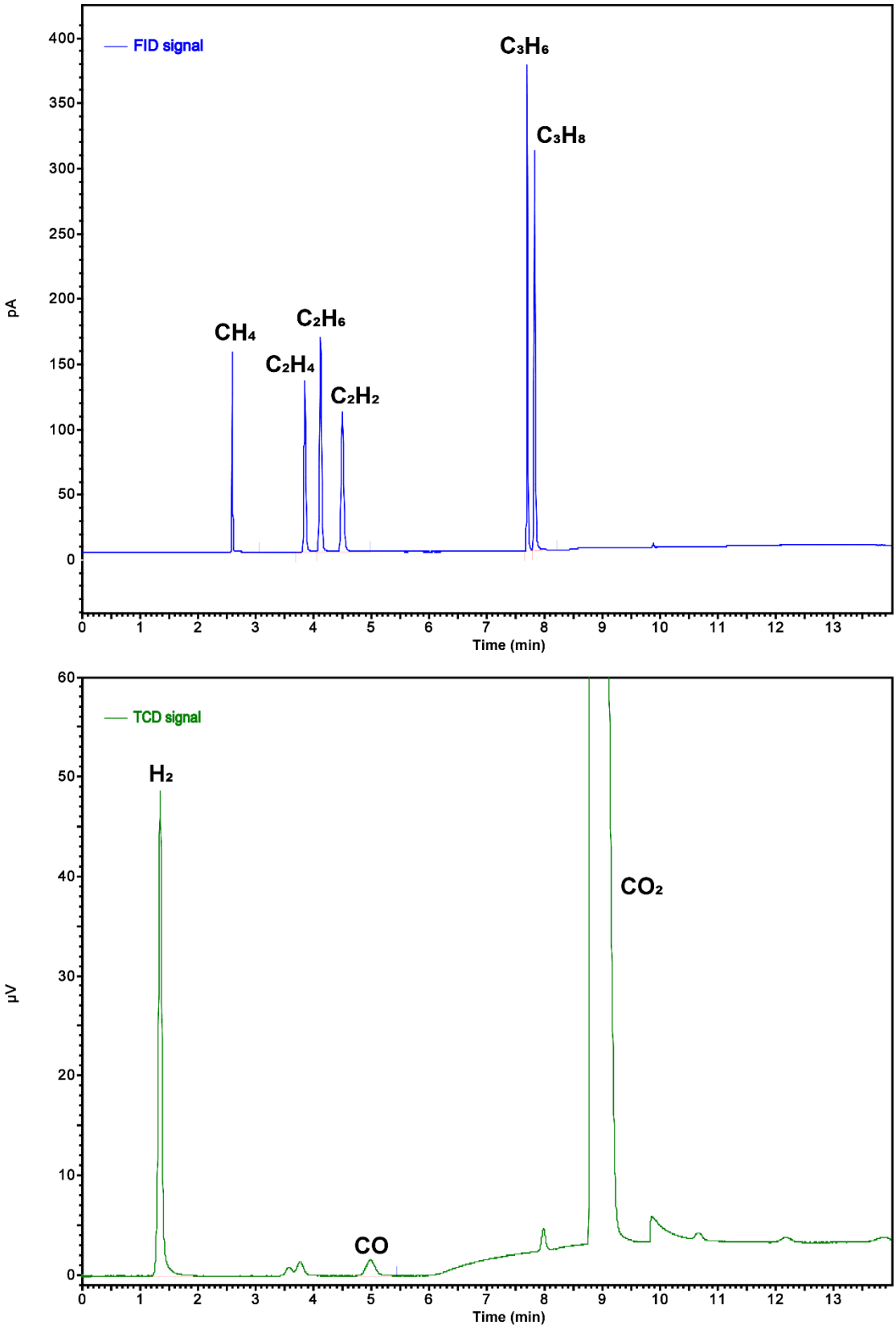

The gas chromatogram of FID (blue) and TCD (green) show that all the tested substance can be completely baseline separated.

S2. Synthesis

Synthesis of **NNU-32**. A mixture of CuI (190 mg, 1 mmol) and H_2bptb (135 mg, 0.5 mmol) in 10 mL DMF was charged in a 15 mL Teflon-lined stainless steel container and heat at 180 ºC for 72 h. After cooling at room temperature, dark-brown sheet crystals were obtained.

Synthesis of **NNU-33(S)**. A mixture of $CuSO_4 \cdot 5H_2O$ (15 mg, 0.06 mmol), H_2bptb (5 mg, 0.0135 mmol) and three drops of triethylamine in 5 mL DMA was charged in a 12 mL Pyrex vial and heat at 150 ºC for 72 h. After cooling at room temperature, light-brown block crystals were obtained.

Synthesis of **NNU-33(I)**. 100 mg **NNU-33(S)** crystals were soaked in a 100 mL 1 M KOH solution for 10 h.

Table S1. Crystal data and structure refinement of **NNU-32** and **NNU-33(S)**.

	NNU-32	**NNU-33(S)**
Empirical formula	$C_{163}H_{106}Cu_{16}N_{65}O$	$C_{80}H_{52}Cu_{10}N_{32}O_5S$
Formula weight	4007.76	2206.98
Crystal system	triclinic	tetragonal
Space group	*P*-1	$P4_12_12$
***a* (Å)**	14.795(4)	15.839(3)
***b* (Å)**	14.838(4)	15.839(3)
***c* (Å)**	34.099(9)	33.754(6)
***α* (°)**	83.986(3)	90
***β* (°)**	86.982(3)	90
***γ* (°)**	84.839(3)	90
***V* (Å^3)**	7407(3)	8468(3)
Z	2	4
D_{calc}**(g·cm^{-3})**	1.796	1.731
Abs.coeff.(mm^{-1})	2.325	2.554
***F*(000)**	4022	4408
Reflns collected	126267/33729	202243/8385
GOFon F^2	1.139	1.137
R_{int}	0.0409	0.0681
R_1[a]	0.0678	0.1405
wR_2**(all data)**[b]	0.1713	0.3271
Flack paremeter	/	0.14

[a] $R_1=\Sigma||F_o|-|F_c||/\Sigma|F_o|$. [b] $wR_2=|\Sigma w(|F_o|^2-|F_c|^2)|/\Sigma|w(F_o^2)^2|^{1/2}$

Table S2. Selected bond distance (Å) of **NNU-32**.

Atom1	Atom2	Length/Å
Cu1	N1	2.036(7)
Cu1	N3	2.133(7)
Cu2	N4	1.892(6)
Cu2	N17	2.372(7)
Cu3	N6	1.838(6)
Cu3	N19	1.860(6)
Cu4	N7	1.924(6)
Cu4	N8	2.263(7)
Cu5	N15	2.014(7)
Cu5	N16	2.141(8)
Cu5	N22	2.064(7)
Cu5	N24	2.060(7)
Cu6	N11	1.889(7)
Cu6	N27	1.882(7)
Cu7	N12	1.892(6)
Cu7	N29	1.870(6)
Cu8	N14	1.878(7)
Cu8	N30	1.893(7)
Cu8	N32	2.348(7)

Table S3. Selected bond distance (Å) of **NNU-33(S)**.

Atom1	Atom2	Length/Å
Cu1	N1	2.34(2)
Cu1	N2	1.97(2)
Cu2	N3	1.89(2)
Cu2	N11	1.89(2)
Cu3	N5	1.89(2)
Cu3	N7	1.94(2)
Cu4	N6	2.11(2)
Cu4	N8	1.96(2)
Cu4	N14	1.83(2)
Cu5	N7	1.94(2)
Cu5	N15	1.93(2)

S3. Computational studies

In this work, the {Cu_8} cluster was chosen as the computational model to reveal the interactions between the up-down Cu(I)-Cu(I) involved in the **NNU-32** and **NNU-33** systems, and further investigate its CO_2RR activity. All DFT calculations were performed with the Gaussian 09 package[5]. We used the M06 hybrid functional, LANL2DZ pseudo-potential with double polarization for Cu, while for those nonmetal atoms (C, O, N, and H) the 6-31G** basis set are used[6-8]. The PCM implicit model was included to simulate the effect of the solvent[9].

To characterize the nature of the Cu(I)-Cu(I), the topology of electron density within the quantum theory of atoms in molecules (QTAIM) developed by R. F. Bader has been performed in Multiwfn software[10,11]. This theory establishes that a chemical bond exists if a line of a locally maximum electron density links two neighboring atoms and also if along that line there is a bond critical point (BCP). The value of the electron density (ρ_{bcp}) and the Laplacian of electron density ($\bigtriangledown^2\rho_{bcp}$) are used to define the interactions present in the molecules. For covalent interactions, the ρ_{bcp} and $\bigtriangledown^2\rho_{bcp}$ are high and negative at the BCP, while for the closed-shell interactions own a small value of ρ_{bcp} and a positive $\bigtriangledown^2\rho_{bcp}$. However, in the case of metal-metal bonds, the ρ_{bcp} and $\bigtriangledown^2\rho_{bcp}$ sometimes are not sufficient to characterize the nature of an interaction in the complex with transitio metal involved in[12]. Therefore, the total energy density (H_c) suggested by Cremer and Kraka was applied as a specific indicator in the analysis of the bonds with transition metal included in[13]. The Espinosa, Varadwaj et al. have proposed that the $|V(r)|/G(r)$ ratio[14-16], where ($V(r)$ is potential energy density and $G(r)$ is kinetic energy density at the BCP, can be used as a better way to characterize a bond, with $|V(r)|/G(r) < 1$ ($\bigtriangledown^2\rho_{bcp} > 0$, $H_c > 0$) for the pure "closed-shell interactions", those with $|V(r)|/G(r) > 2$ ($\bigtriangledown^2\rho_{bcp} < 0$, $H_c < 0$) are typical "covalent interactions", while for $1 < |V(r)|/G(r) < 2$ (($\bigtriangledown^2\rho_{bcp} > 0$, $H_c < 0$) are of "intermediate character".

Proton-coupled electron transfer (PCET) steps were considered in the electrochemical process of $CO_2 + 8H^+ + 8e^- \rightarrow CH_4 + 2H_2O$ by using the computational hydrogen electrode (CHE) model pioneered by Nørskov et al[17]. In this model, the proton-electron pair is equal to half of the chemical potential of the hydrogen molecule.

The periodic calculations are performed within the framework of DFT implemented in the Vienna ab initio simulation package (VASP).[18-20] The generalized gradient approximation with the functional is described by the Perdew-Burke-Ernzerhof type (PBE).[21] The projector-augmented wave (PAW) method[22] is applied to describe the wavefunctions in the core regions, while the valence wavefunctions are expanded as linear combination of plane-waves with a cutoff energy of 400 eV. The total energy is converged to 10^{-5} eV in the geometry optimizations, and the Hellmann–Feynman force on each relaxed atom is less than 0.02 eV/Å. The {Cu_8} fragment is placed in a periodic box with the size of 30*30*40 as shown below. To simulate a charged cell, the negative charge is added to the system and the compensating charge is placed in the electrolyte which is approximated by a polarizable dielectric continuum (i.e., an

implicit solvation model) with VASPsol[23,24]. The applied potential is obtained by $U = \Phi - \Phi_{SHE}$, where Φ denotes for the work function and the Φ_{SHE} refers to a reference energy of 4.6 V[23].

The AIMD simulations were performed by the CP2K code with PBE functional.[25,26] The valence electrons were described by double-ζ basis sets of the MOLOPT type and the core parts are represented by Goedecker−Teter−Hutter pseudopotentials, respectively.[27,28] The dispersion interactions were also taken into account with D3 method by Grimme.[29] The self-consistent continuum solvation (SCCS) model was adopted to account for the solvation effect.[30-32] The time step was fixed at 0.5 fs and the temperature maintained at 300 K using a Nosé–Hoover thermostat chain.[33]

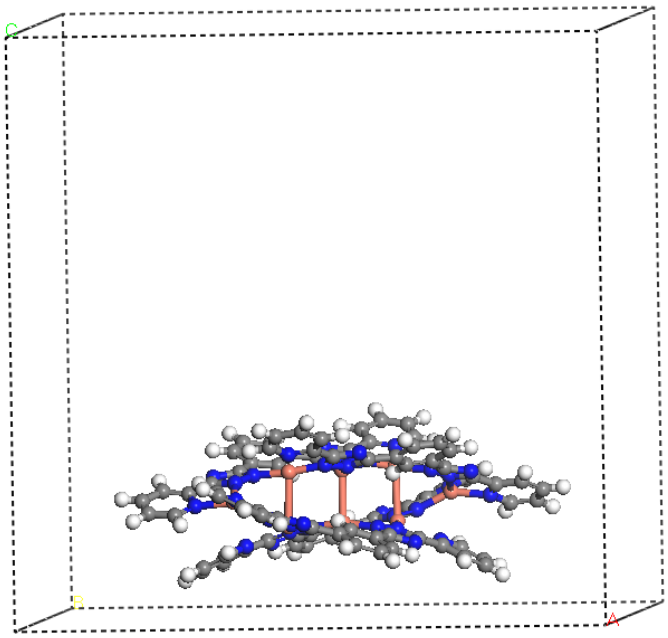

Applied periodic box and structure for the periodic calculations.

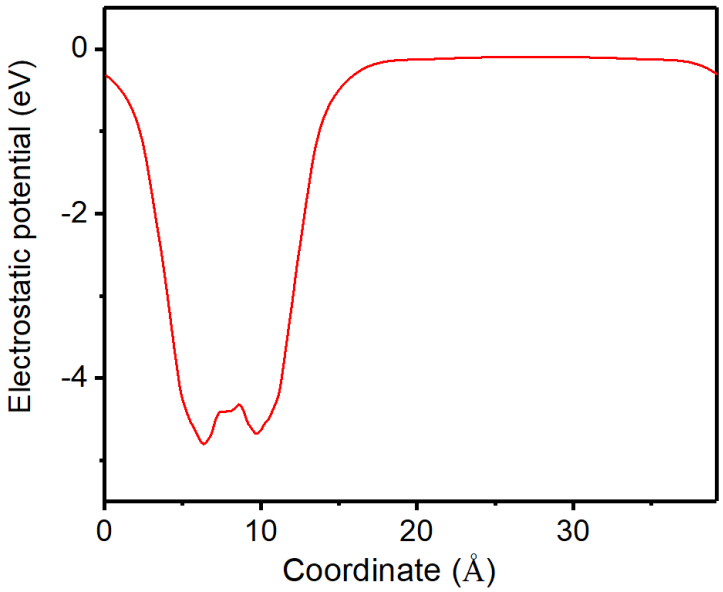

Calculated electrostatic potential along with z direction for the periodic calculations, the work function is then can be calculated.

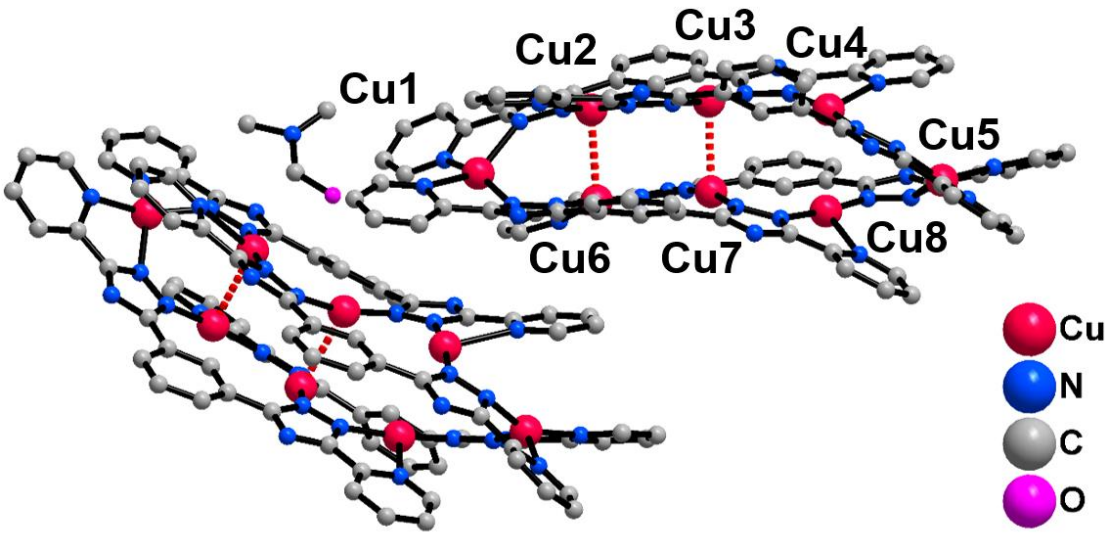

Figure S1. The asymmetric unit of **NNU-32**. **NNU-32** consists of two {Cu_8} clusters and one DMF molecular. All hydrogen atoms are omitted for clarity.

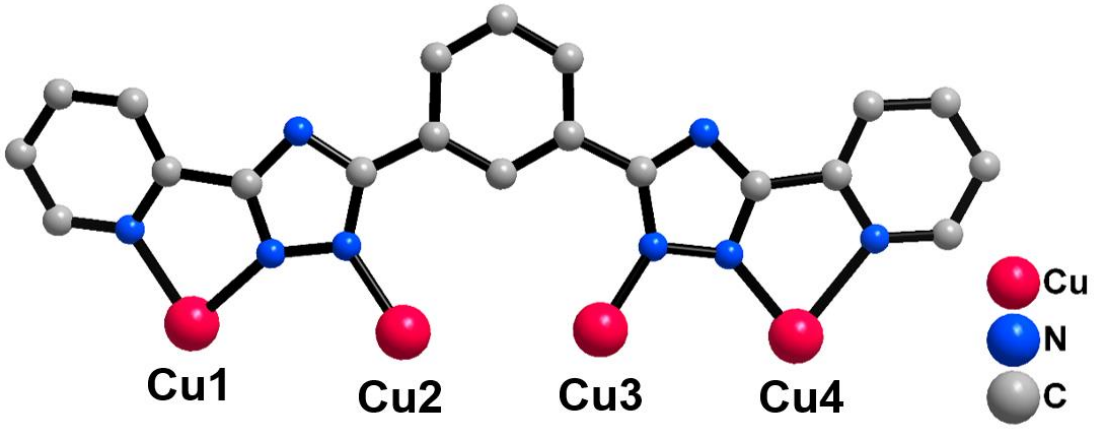

Figure S2. The coordination environment of ligands in **NNU-32**. Each $bptb^{2-}$ has two pyridine nitrogens and four triazole nitrogens coordinates with four Cu(I) ions.

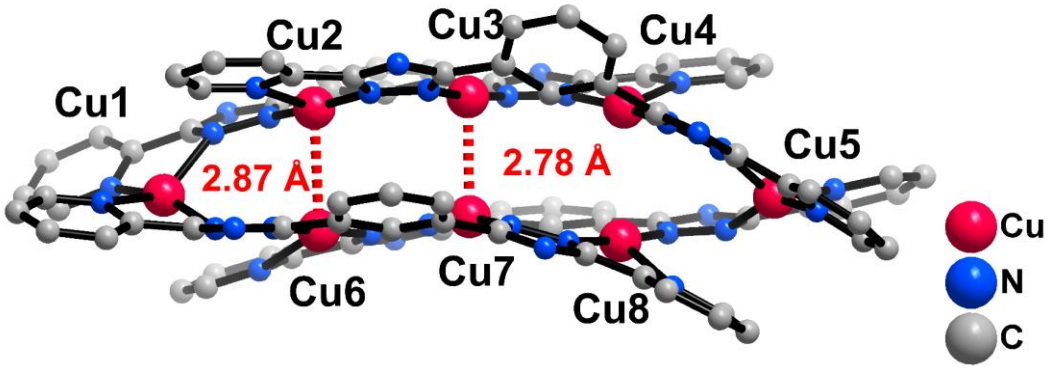

Figure S3. Cuprophilic interactions in **NNU-32**. All the Cu ions are coordinated with N atoms from $bptb^{2-}$ ligands in three different coordination types: two Cu ions (Cu1 and Cu5) assume compressed tetrahedral coordination geometry; four Cu ions (Cu2, Cu4, Cu6 and Cu8) take triangular shapes; the rest two Cu ions (Cu3 and Cu7) are in linear coordinated configuration. Combine coordination geometry with charge balance, the oxidation states of all the Cu ions are calculated to be Cu(I).

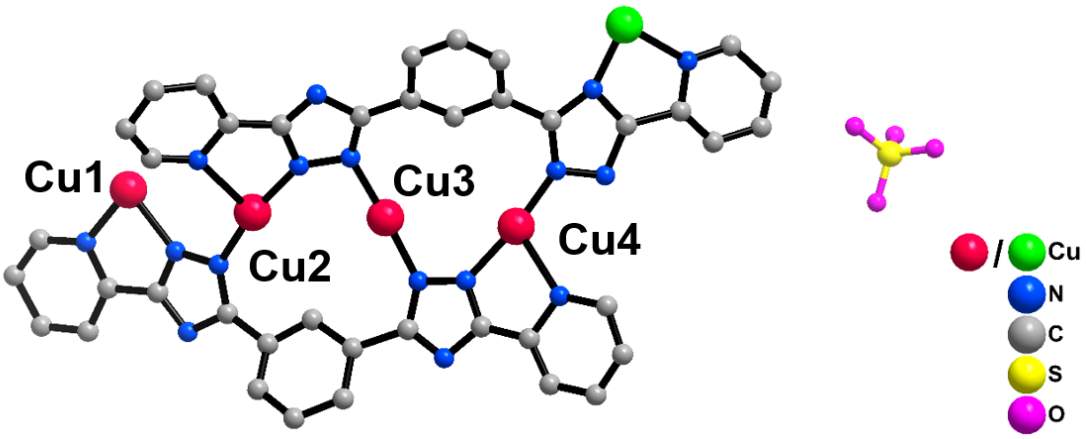

Figure S4. The asymmetric unit of **NNU-33(S)**. All H atoms are omitted for clarity. Color code: Cu, red and green; N, blue; C, gray; S, yellow; O, pink.

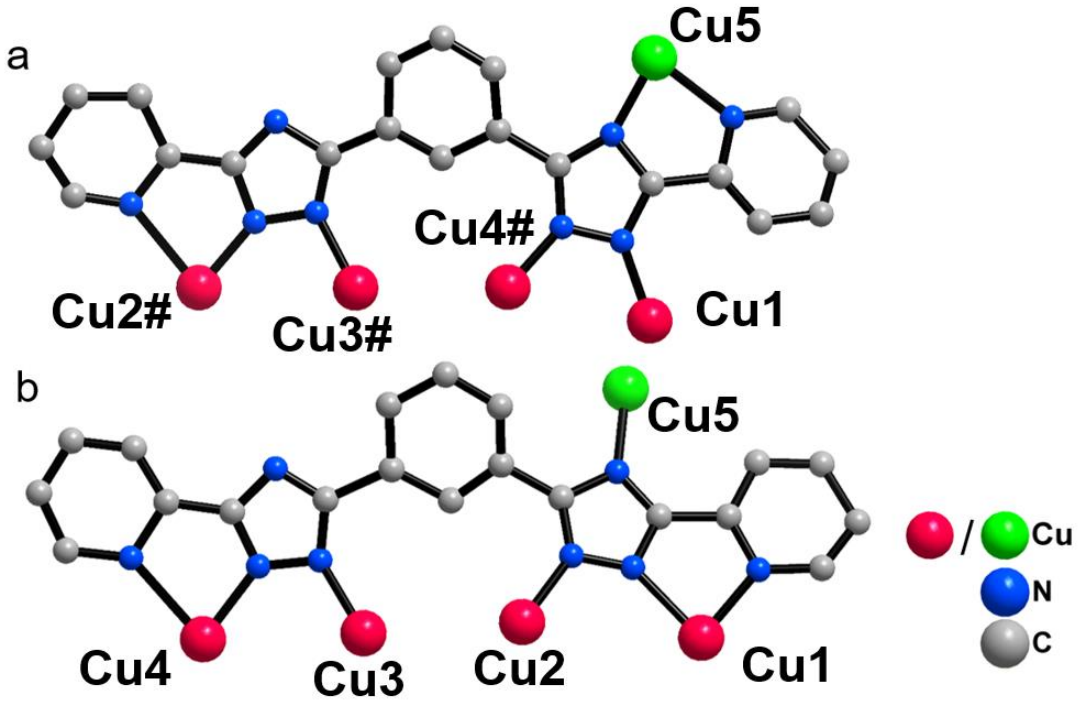

Figure S5. The coordination environment of ligands in **NNU-33(S)**. Each $bptb^{2-}$ coordinates with five Cu(I) ions. Due to the overturn of terminal pyridine ring, the environment of ligands in **NNU-33(S)** have **a** and **b** two kinds coordination environment.

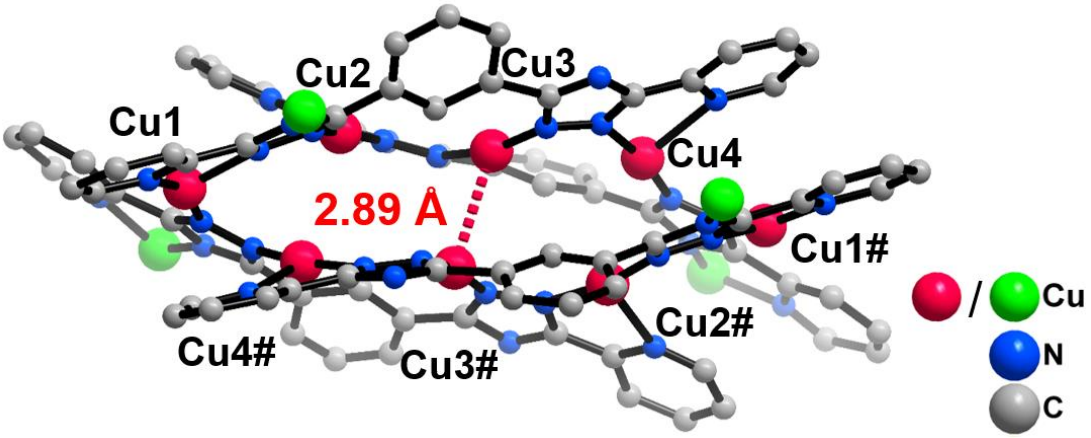

Figure S6. Cuprophilic interaction in **NNU-33(S)**. All the linker Cu ions in green are Cu5.

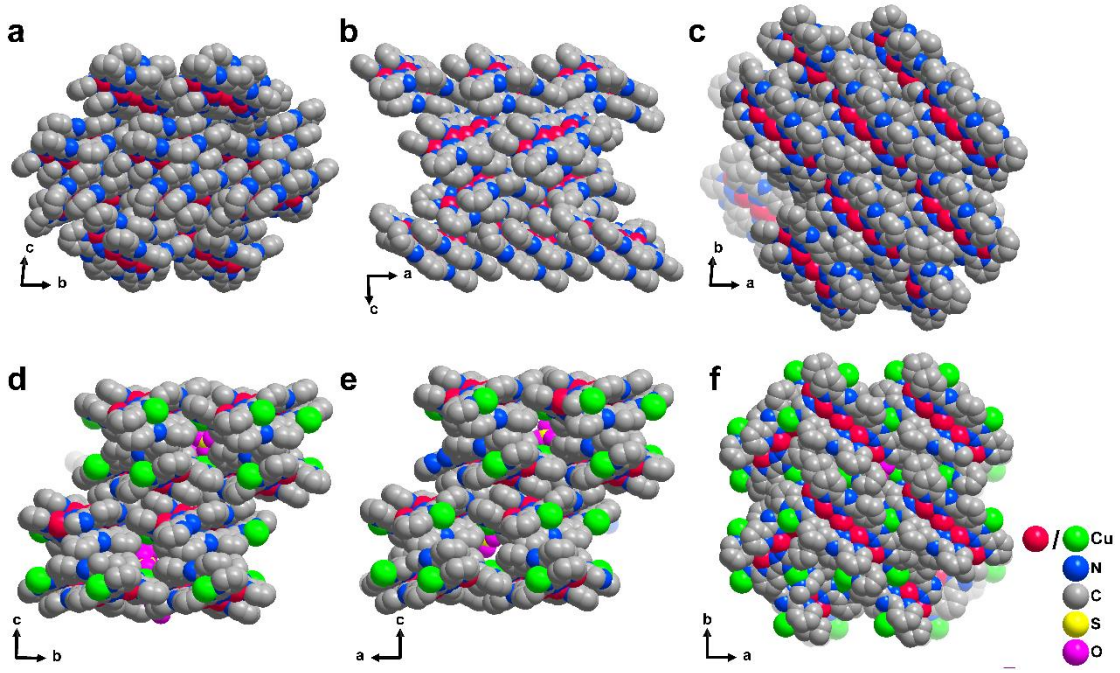

Figure S7. a-c. Packing diagram of **NNU-32** along *a*, *b* and *c* axis. **d-f.** Packing diagram of **NNU-33(S)** along *a*, *b* and *c* axis.

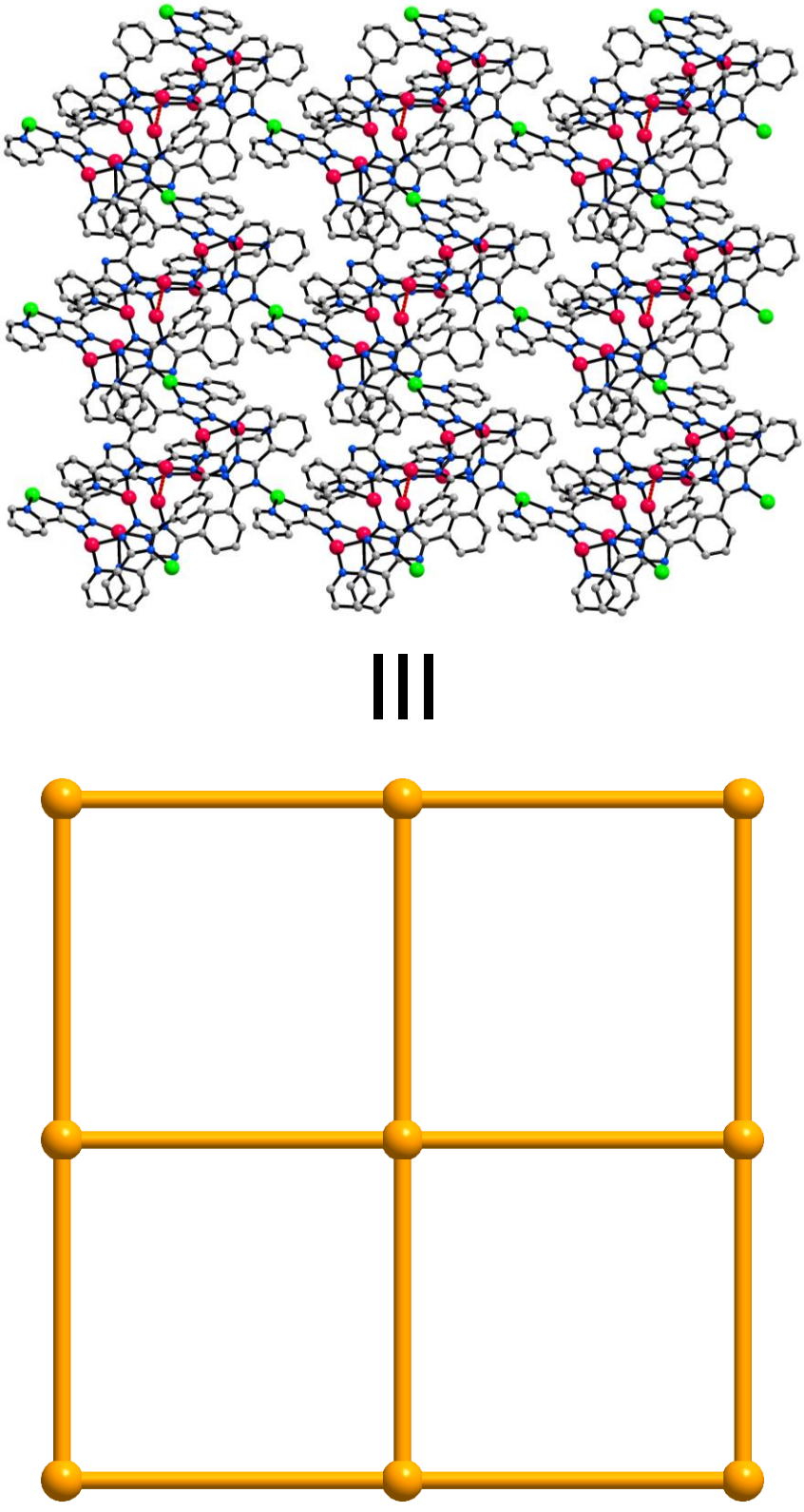

Figure S8. The single layer and responding sql topos of **NNU-33(S)**

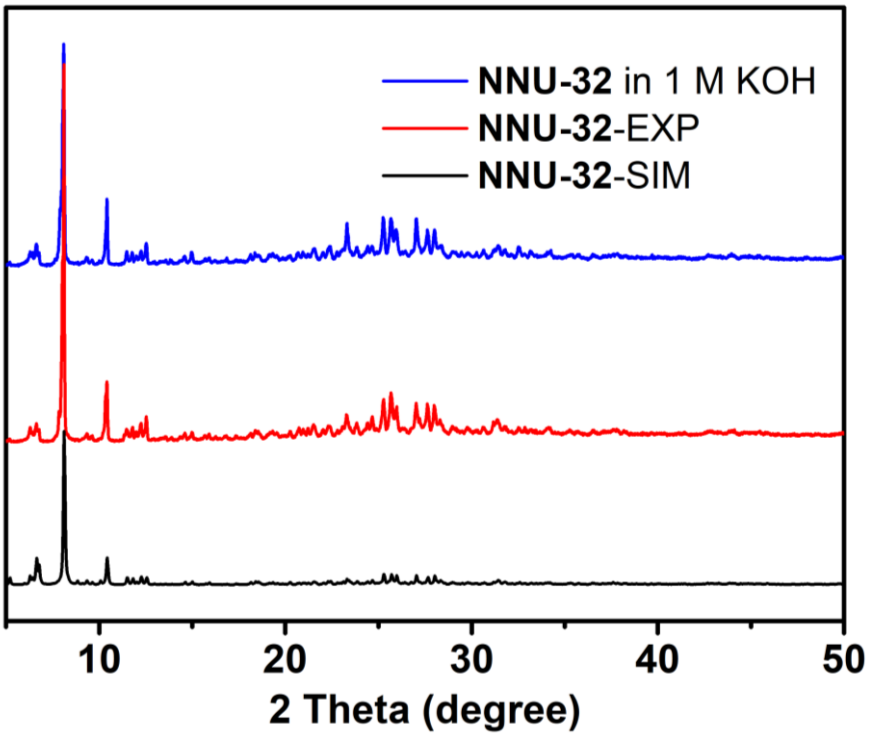

Figure S9. PXRD patterns of simulated (black), experimental (red) and after soaking in 1 M KOH solution (blue) of **NNU-32**.

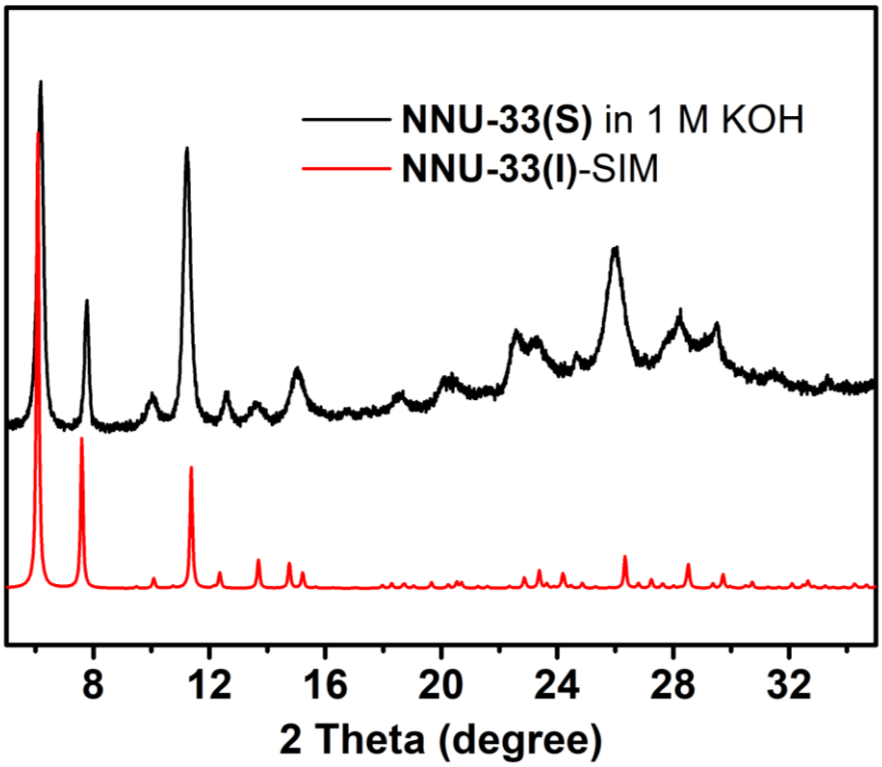

Figure S10. PXRD patterns for simulated **NNU-33(I)** and **NNU-33(S)** after soaking in 1 M KOH solution. There are some slight differences before 12° and near 26°.

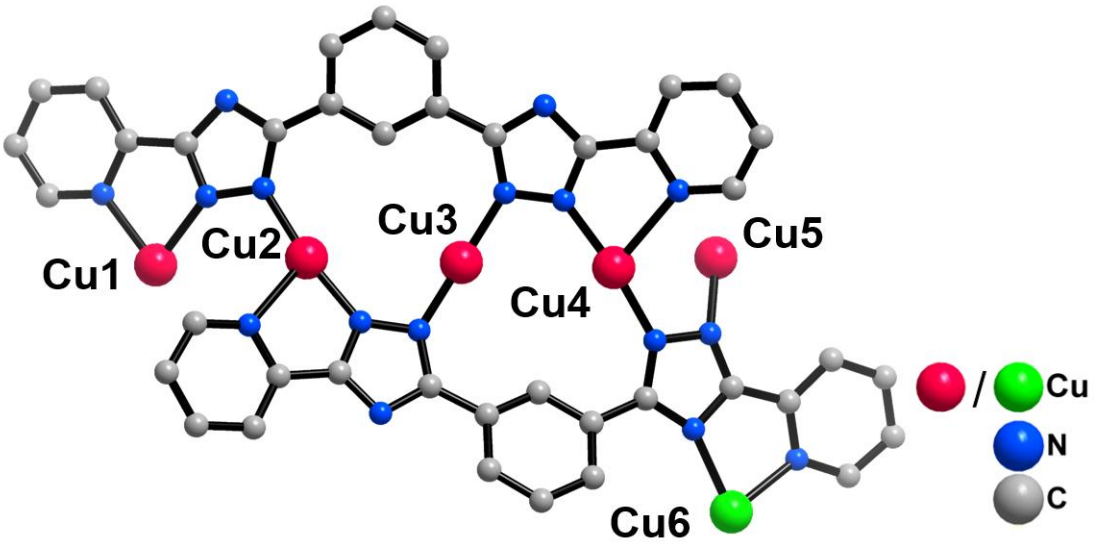

Figure S11. The asymmetric unit of **NNU-33(H)**. All H atoms are omitted for clarity.

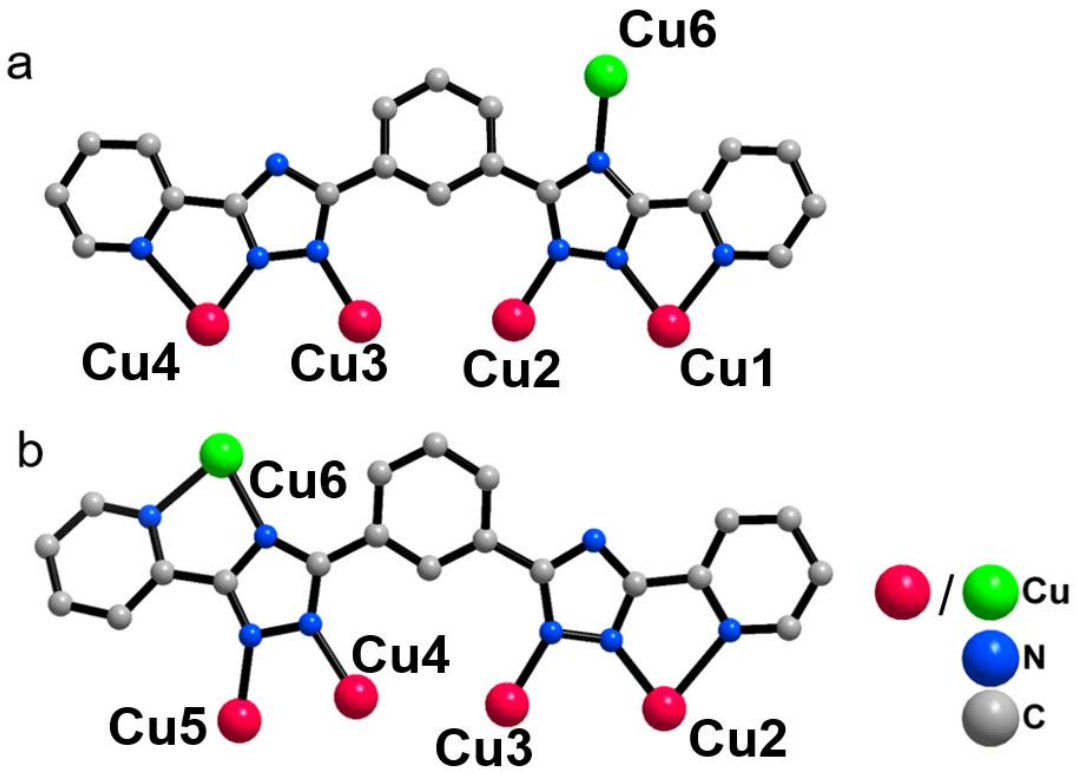

Figure S12. Two kinds of coordination environment of ligands in **NNU-33(H)**, which is similarly to **NNU-33(S)**.

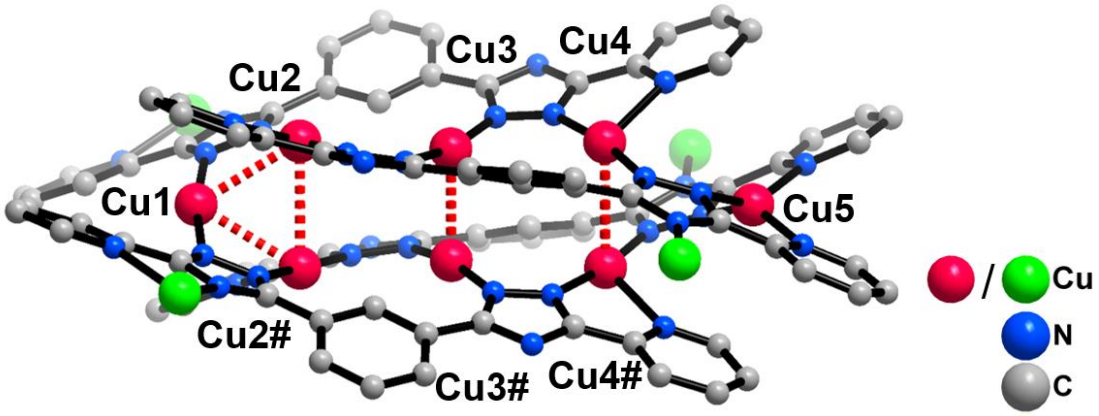

Figure S13. Cuprophilic Interaction in **NNU-33(H)**.

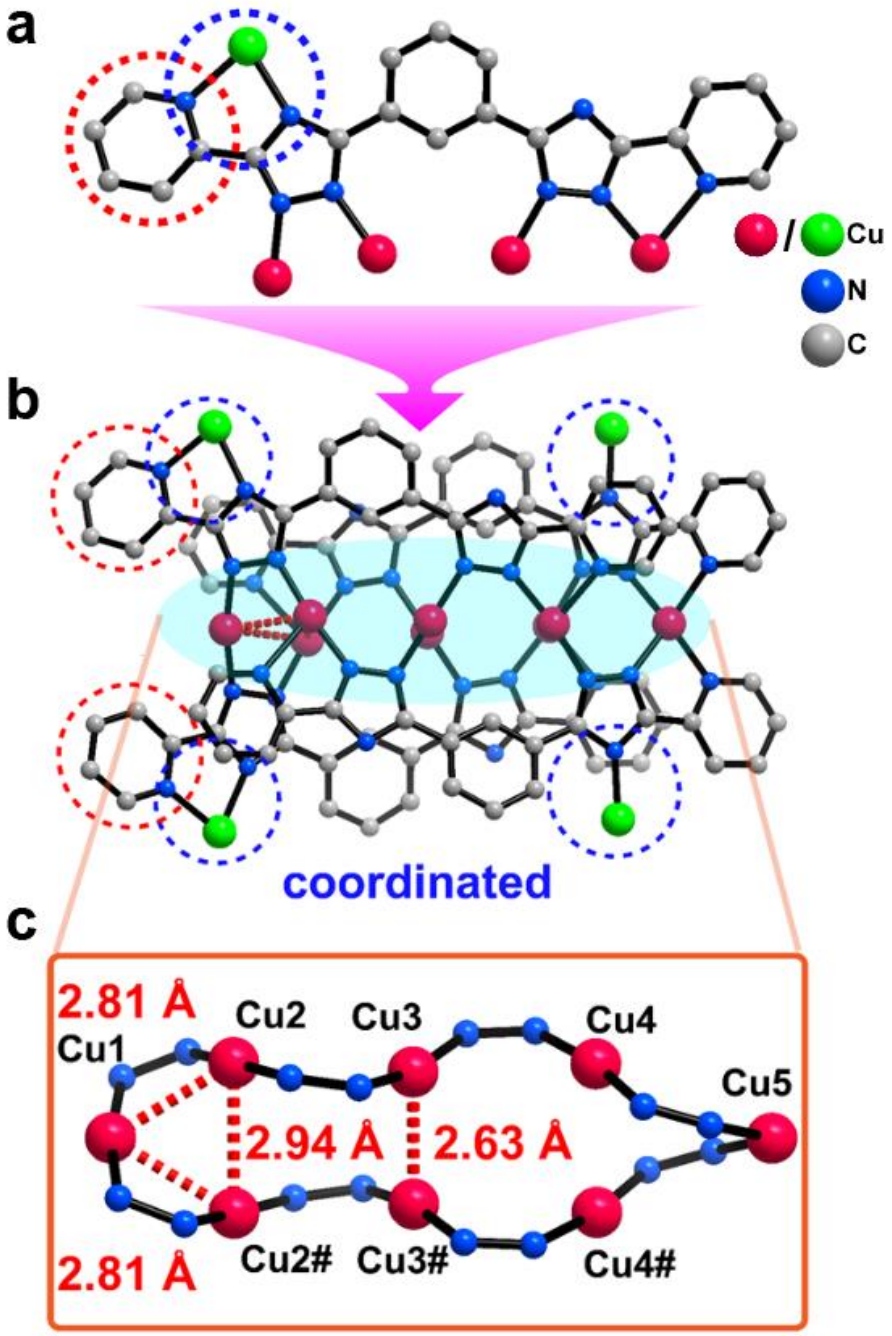

Figure S14. The detail structural composition of **NNU-33(H).**

Table S4. Comparison of cell parameters among **NNU-33(S)**, **NNU-33(I)** and **NNU-33(H)**

	NNU-33(S)	**NNU-33(I)**	**NNU-33(H)**
Molecular formula	$C_{80}H_{52}Cu_{10}N_{32}O_5S$	$C_{80}H_{52}Cu_{10}N_{32}O_2$	$C_{80}H_{52}Cu_{10}N_{32}O_2$
Formula weight	2209	2129	2129
Length of *a* axis	15.839	16.441	16.336
Length of *b* axis	15.839	16.441	16.336
Length of *c* axis	33.754	31.090	31.552
Volume	8468	8403	8419
Counter ion	SO_4^{2-}	OH^-	OH^-

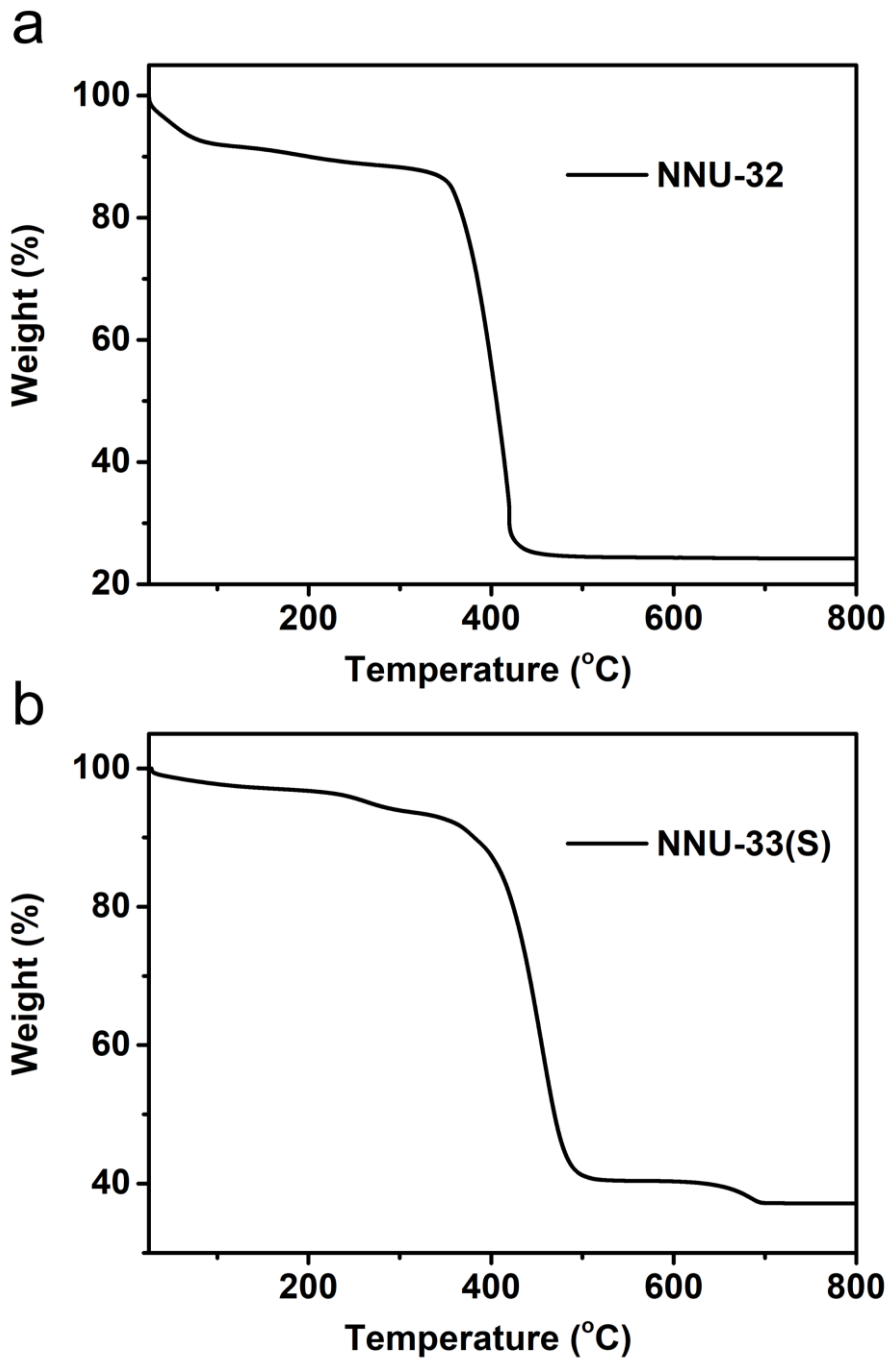

Figure S15. Thermogravimetry curves of **a NNU-32** and **b NNU-33(S)** measured in N_2/O_2 from room temperature to 800 °C at the heating rate of 20 °C·min^{-1}, respectively. Both of **NNU-32** and **NNU-33** show great thermostabilities over 300 °C.

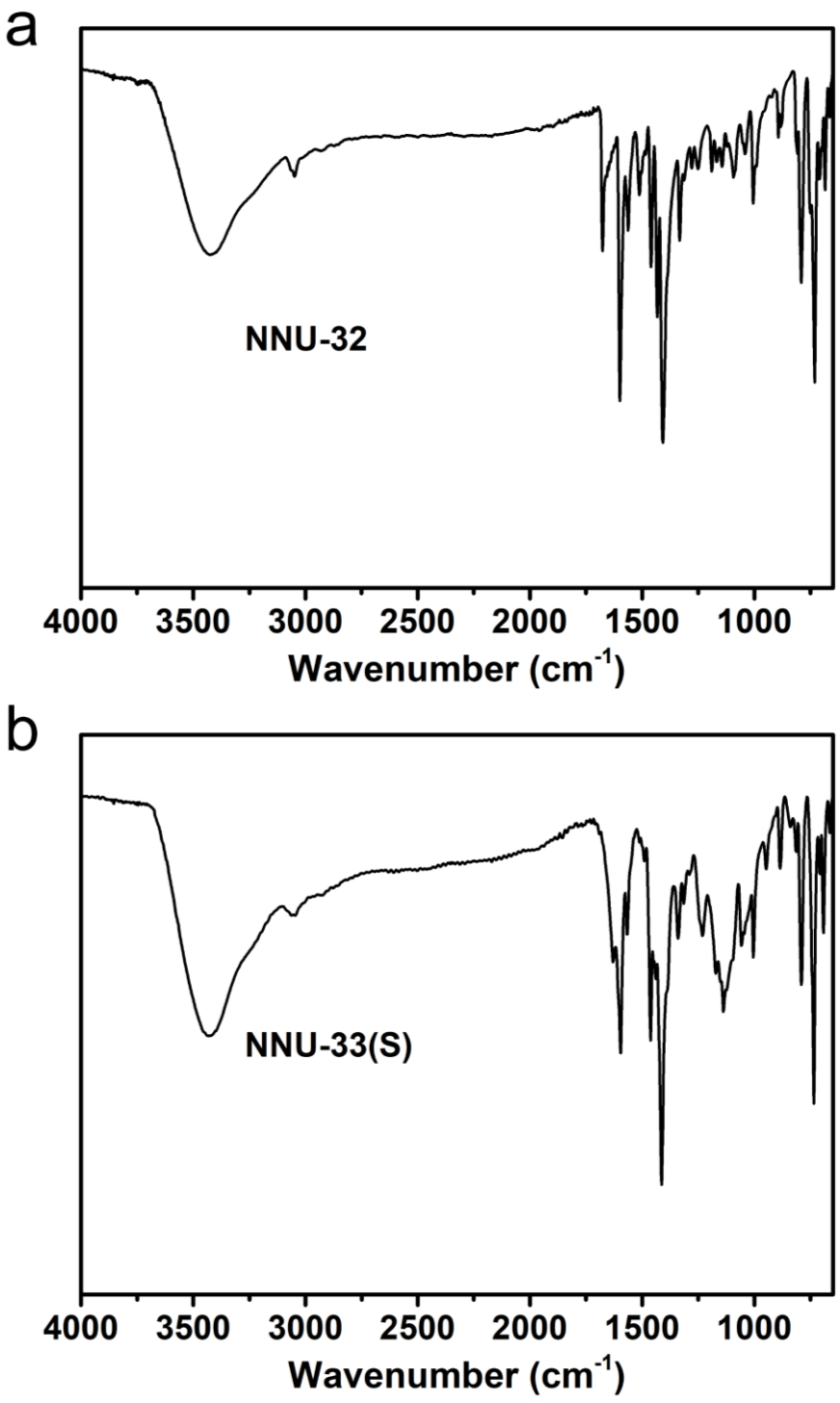

Figure S16. The FTIR spectra for **a NNU-32** and **b NNU-33(S)**, respectively.

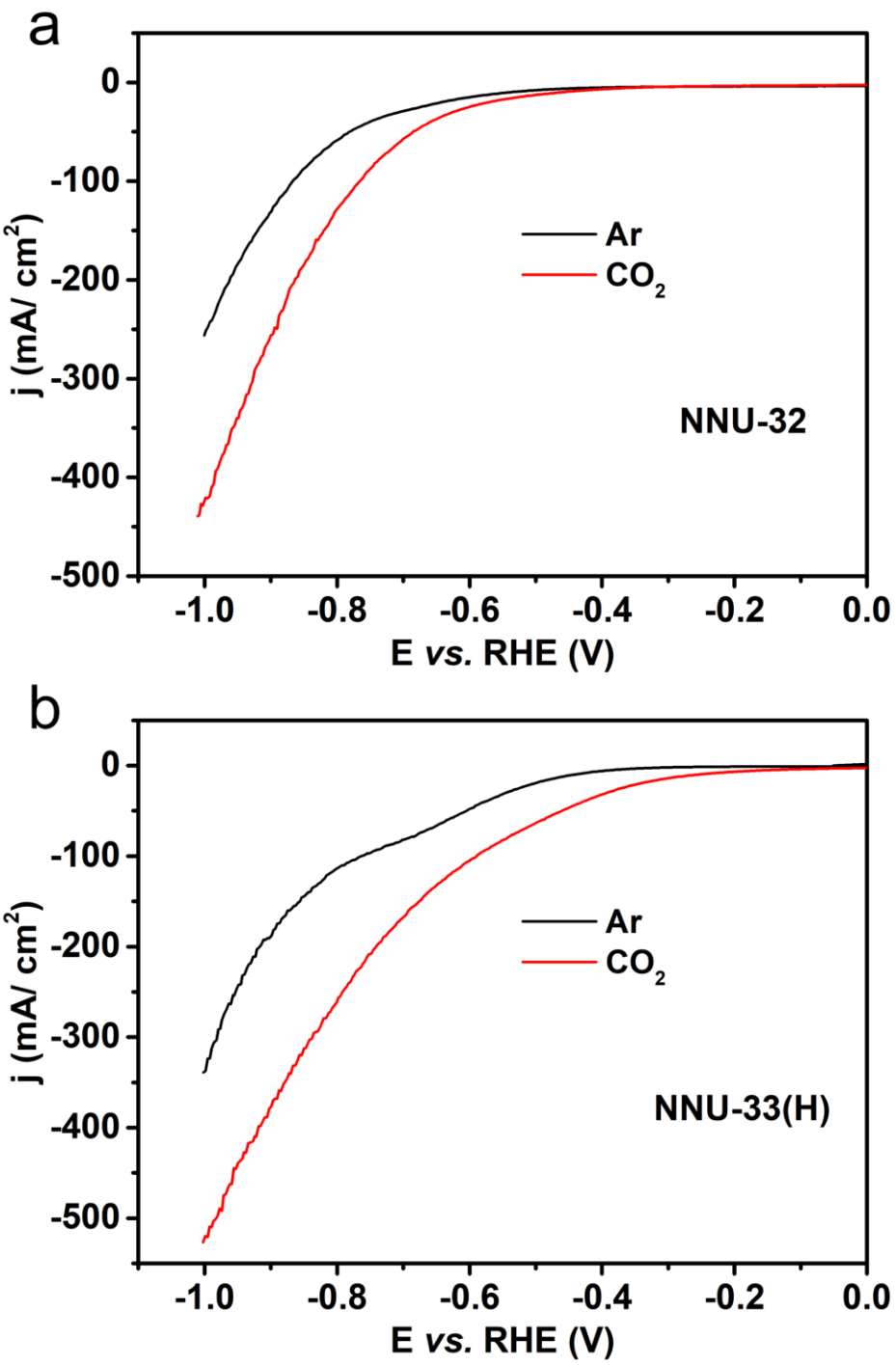

Figure S17. Linear sweep voltammetric curves of **a NNU-32** and **b NNU-33(H)** under Ar flow and CO_2 flow in 1 M KOH aqueous solution, respectively.

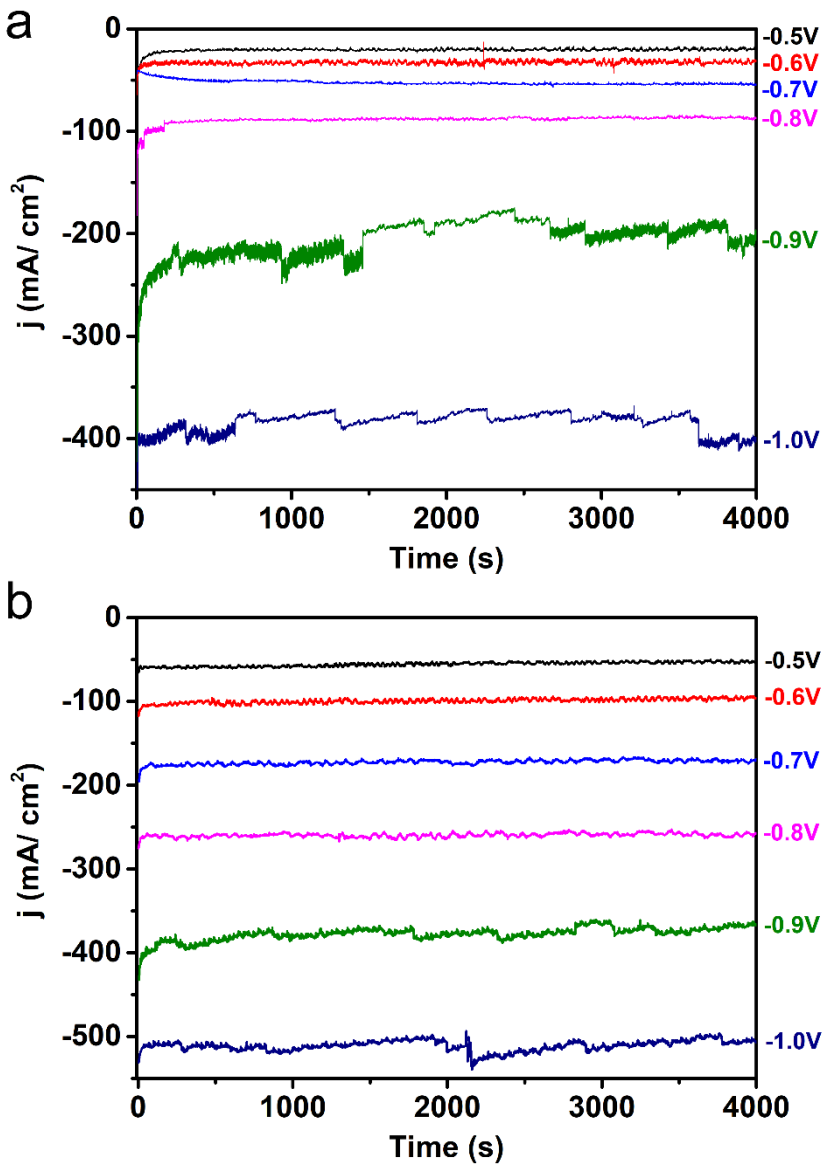

Figure S18. Chronoamperometric curves at various potentials for CO_2 reduction on **a NNU-32** and **b NNU-33(H)** in 1 M KOH electrolyte, respectively.

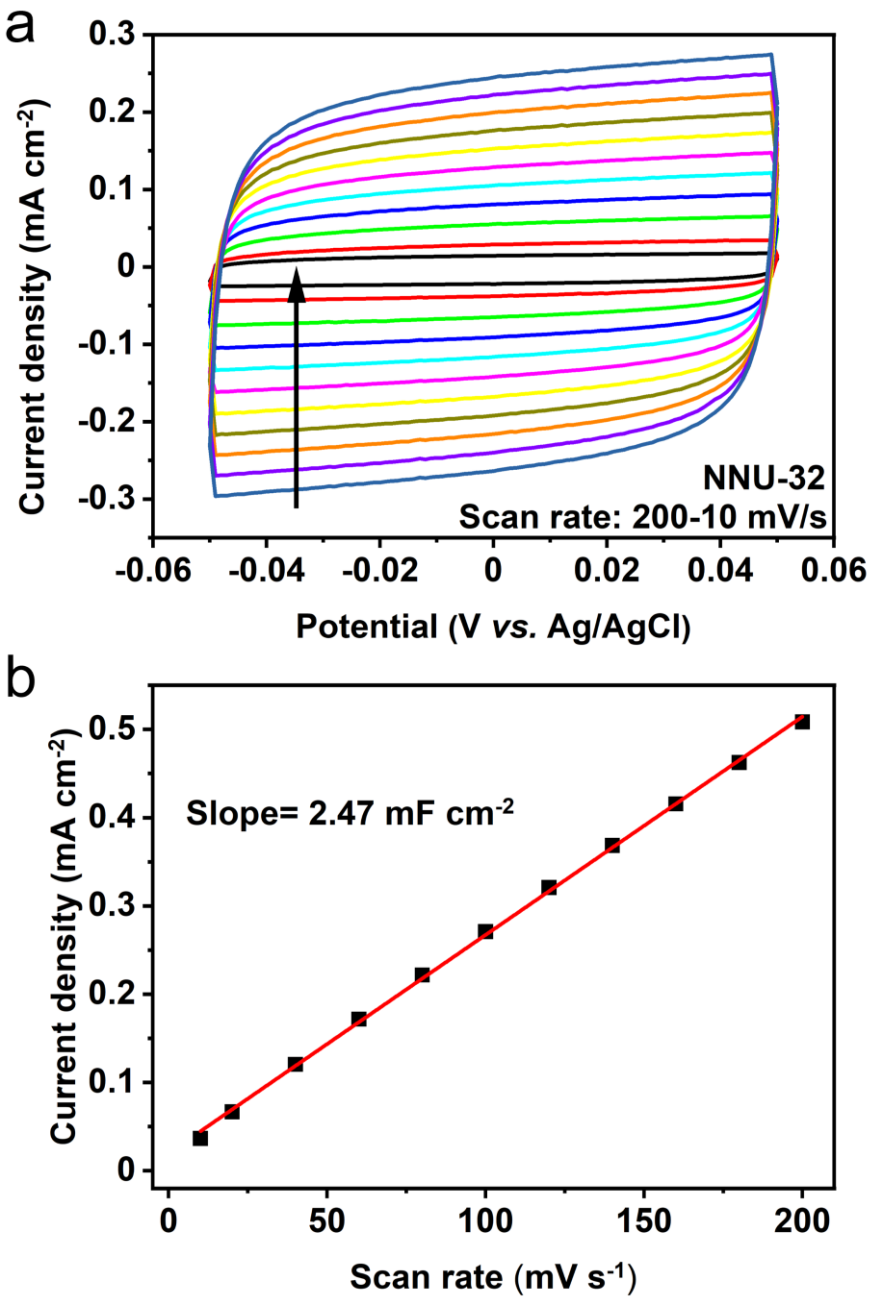

Figure S19. Cyclic voltammertrys (CV) curves in the region of -0.05 ~0.05 V *vs.* RHE at various scan rate (10 ~ 200 mV s^{-1}) and corresponding capacitive current of **NNU-32**.

The Tafel slopes are calculated based on Tafel equation ($\eta = b \log j + a$, where η is the overpotential, j is the current density and b is the Tafel slope).

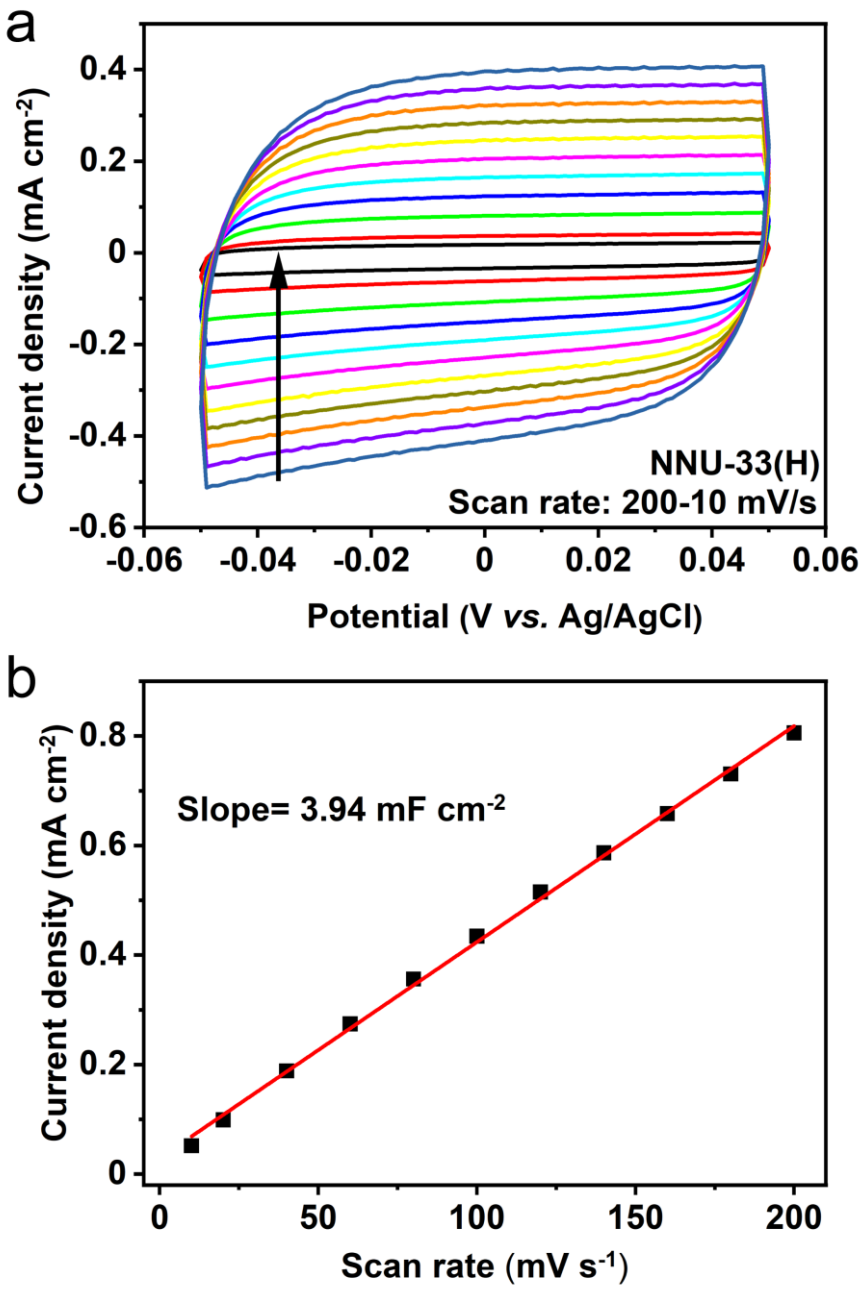

Figure S20. Cyclic voltammertrys (CV) curves in the region of -0.05 ~0.05 V *vs.* RHE at various scan rate (10 ~ 200 mV s^{-1}) and corresponding capacitive current of **NNU-33 (H)**.

Table S5. The cell resistances with different electrocatalysts.

Sample	Resistance (Ω)
NNU-32	**5.3**
NNU-33(H)	**4.2**

Table S6. The detail values of faradic efficiency catalyzed by **NNU-32**.

V *vs.* RHE	H_2 (%)	CO (%)	CH_4 (%)	C_2H_4 (%)	HCOOH(%)	CO_2RR (%)
-0.5	50.78±6.32	44.46±5.47	1.14±0.22	3.92±0.47	0.88±0.34	50.4±4.54
-0.6	45.72±5.24	42.02±5.36	4.69±0.94	6.01±1.11	1.04±0.22	53.76±3.53
-0.7	35.21±3.49	33.53±2.48	23.11±1.36	6.16±0.73	1.11±0.48	63.91±3.08
-0.8	33.12±2.15	15.54±1.61	41.7±3.99	6.69±0.56	1.22±0.15	65.15±4.27
-0.9	40.74±3.48	2.65±0.73	53.12±5.72	3.37±0.12	<0.01	59.14±3.85
-1.0	40.41±3.01	1.57±0.59	55.1±6.37	2.1±0.25	<0.01	58.77±4.73

Table S7. The detail values of faradic efficiency catalyzed by **NNU-33(H)**.

V *vs.* RHE	H_2 (%)	CO (%)	CH_4 (%)	C_2H_4 (%)	HCOOH(%)	CO_2RR (%)
-0.5	30.78±4.19	64.46±5.43	1.14±0.23	3.92±0.96	0.75±0.21	70.27±3.97
-0.6	29.32±4.23	58.41±5.74	3.92±1.12	7.62±1.02	0.36±0.15	70.31±3.41
-0.7	11.34±1.73	25.1±3.12	35.1±2.34	27.71±3.55	0.11±0.06	88.02±4.64
-0.8	10.82±1.84	17.39±3.07	54.66±3.75	18.85±3.67	<0.01	90.9±4.15
-0.9	6.58±2.98	6.1±1.11	82.17±4.88	6.04±2.74	<0.01	94.31±3.01
-1.0	12.24±3.72	11.83±2.52	63.19±4.67	13.6±3.51	<0.01	88.62±3.46

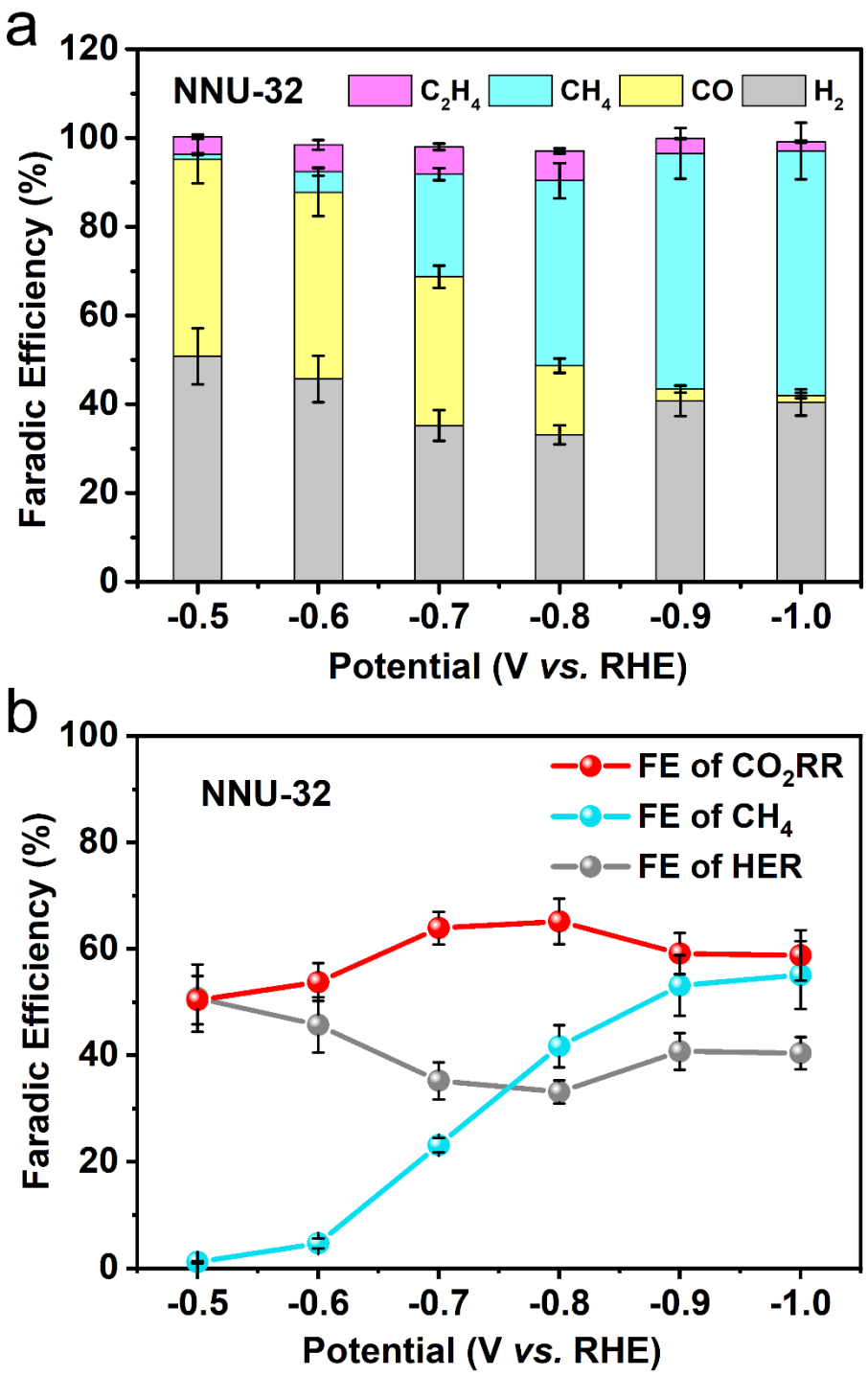

Figure S21. a. Faradic efficiency (FE) of H_2, CO, CH_4 and C_2H_4 products with **NNU-32** as electrocatalyst and **b.** comparison of FE for HER, total CO_2RR and CH_4 conversion catalyzed by **NNU-32.**

Table S8. Comparison of the electrocatalytic CO_2-to-CH_4 activities of the reported Cu-based catalysts.

Catalyst	Reactor type	Electrolyte	Applied potential (V vs. RHE)	Current density (mA cm^{-2})	FE_{CH4} (%)	Reference
NNU-33(H)	Flow cell	1 M KOH	-0.9	391	82.2	This work
NNU-32	Flow cell	1 M KOH	-1.0	384	55.1	This work
La_2CuO_4	Flow cell	1 M KOH	-1.4	117	56.3	34
Cu_{oh}	Flow cell	1 M KOH	-0.91	100	53	35
Cu	H-type	0.5 M $NaHCO_3$	-2.2	38	85	36
Cu clusters/ DRC	H-type	0.1 M $KHCO_3$	-1.0	18	81.7	37
n-Cu/C	H-type	0.1 M $NaHCO_3$	-1.35	7	76	38
CuPc	H-type	0.5 M $KHCO_3$	-1.06	13	66	39
Cu_2O@Cu-MOF	H-type	0.1 M $KHCO_3$	-1.71	/	63.2	40
Cu-CeO_2	H-type	0.1 M $KHCO_3$	-1.8	33.6	58	41
Polished Cu foil	H-type	0.3 M KI + 0.1 M $KHCO_3$	-1.0	6.7	56	42
Cu Nanowires	H-type	0.1 M $KHCO_3$	-1.25	4.4	55	43

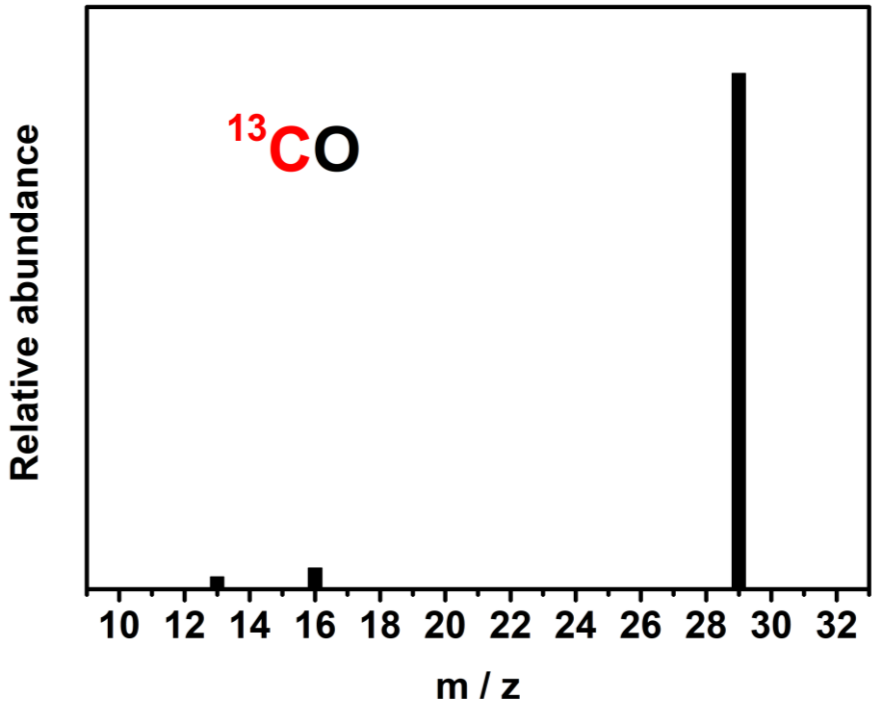

Figure S22. Mass spectra extracted from GC-MS analysis of CO product from $^{13}CO_2$ reduction

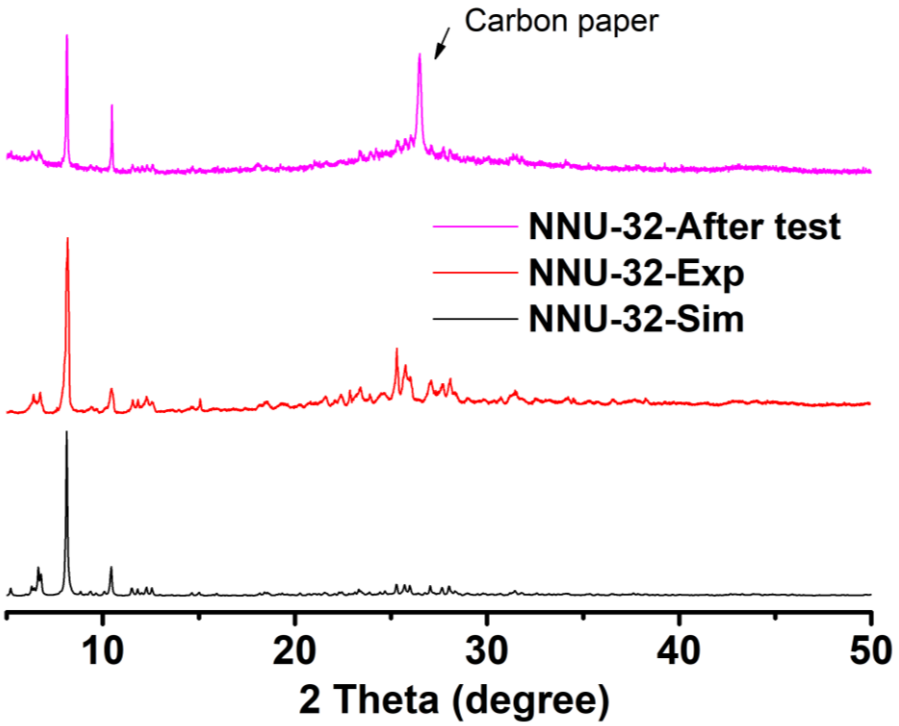

Figure S23. PXRD patterns for obtained **NNU-32**, and **NNU-32** after electrochemical CO_2RR.

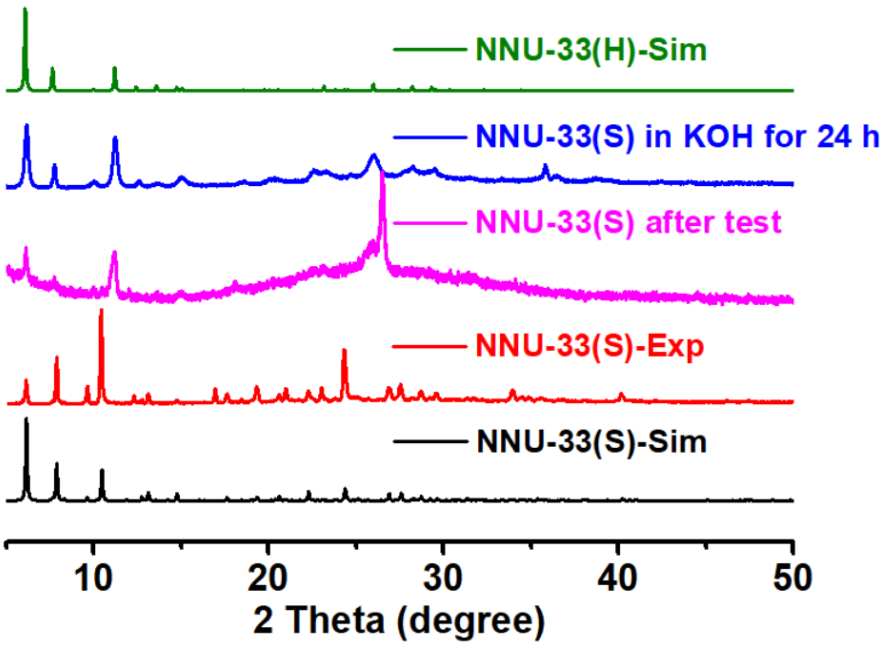

Figure S24. PXRD patterns for obtained **NNU-33(S)**, **NNU-33(S)** after electrochemical CO_2RR, **NNU-33(S)** leaving in 1 M KOH aqueous solution under N_2 environment for 24 h and simulated **NNU-33(H)**.

The well-matched curves between simulated and obtained **NNU-33(S)** sugested the high purity of catalyst. After electrocatalysis, the peak originally located at 10.45 ° almost disppear and a new peak at 11.04 ° generated, which was identical with the curve corresponding to **NNU-33(S)** after soaking in 1 M KOH. The slight difference illustrates that there is single-crystal-to-single-crystal transformation happened for **NNU-33(S)** in alkaline aqueous solution. In addition, the well-matched curves between that of after test and alkali treatment suggest that **NNU-33(S)** indeed convert into **NNU-33(H)** during CO_2RR.

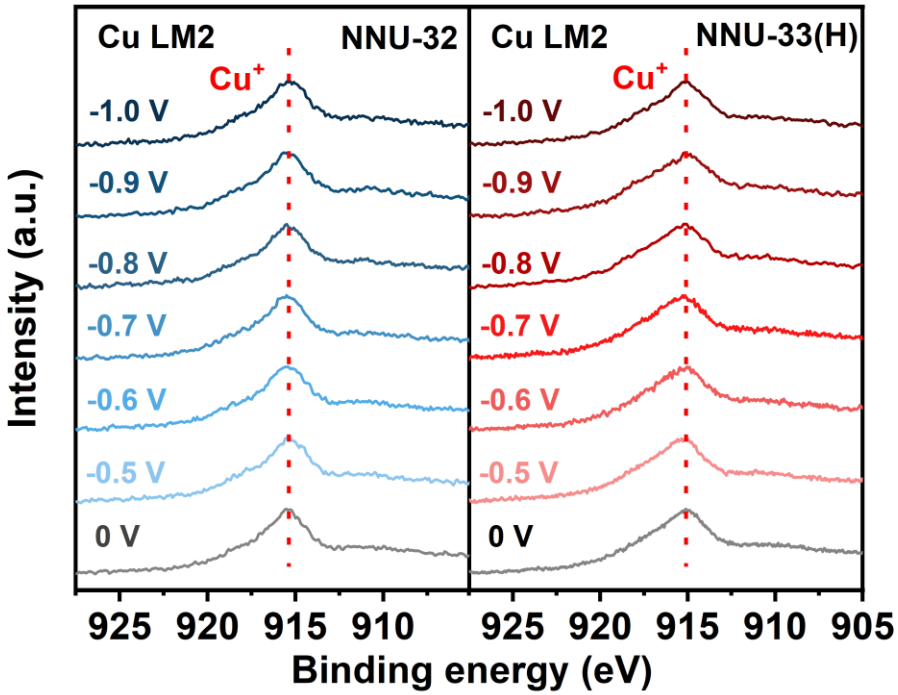

Figure S25. Cu LM2 XPS spectra of **NNU-32** and **NNU-33(H)** before and after CO_2RR under -0.5 ~ -1 V (vs. RHE).

Through comparing the Cu LM2 XPS spectra before and after CO_2RR at a series of applied potentials, the peaks corresponding to Cu(I) were unaltered in all cases, which showed that the oxidant state of Cu(I) could be maintained on the cathode.

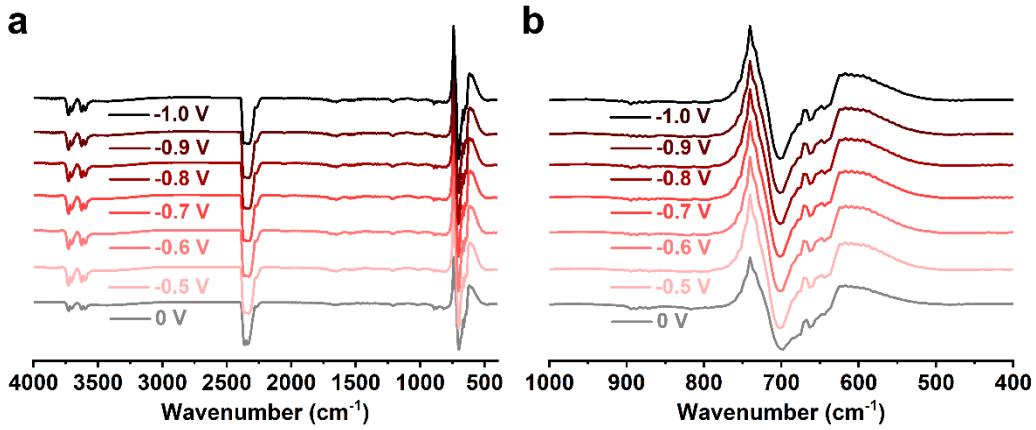

Figure S26. *In situ* FTIR spectra for before and during CO_2RR (-0.5 ~ -1 V vs. RHE) on NNU-33(H). a. 4000-400 cm^{-1}; b. Magnified *in situ* FTIR spectra from 1000 to 400 cm^{-1}.There was no difference of peaks in all cases, which showed the stability of electrocatalysts.

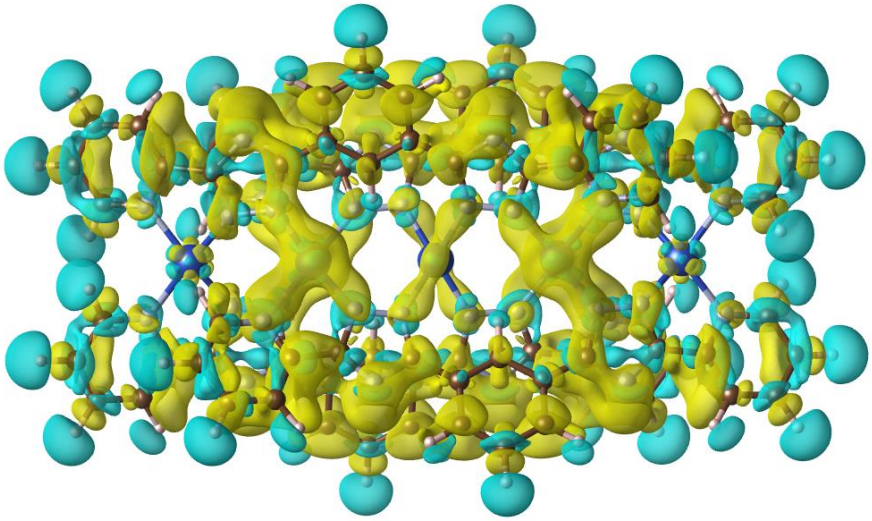

Figure S27. Charge density difference of {Cu_8} between a neutral state and a charged state of -1, isosurface value is set as 0.00035 eV/A^3.

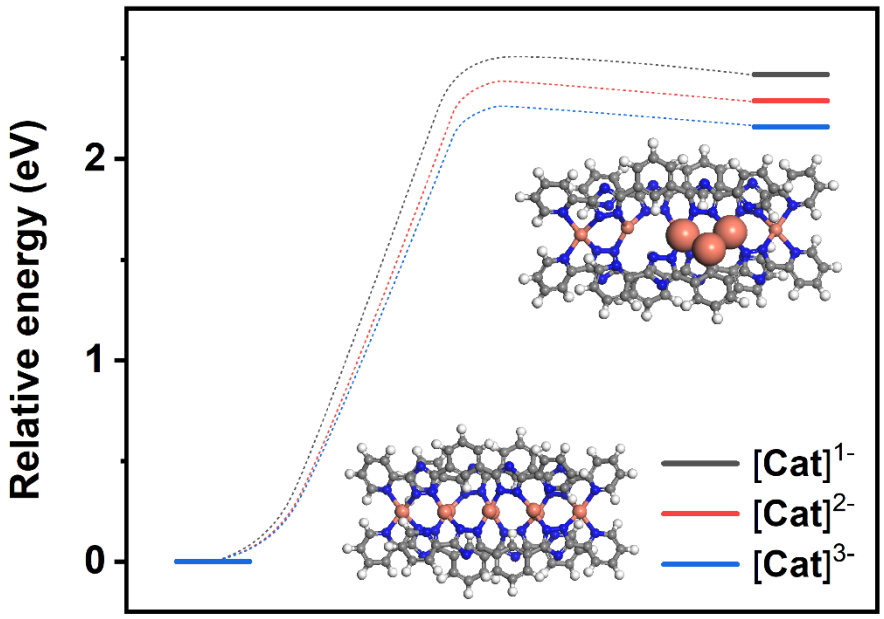

Figure S28. Relative energies of the {Cu_8} fragment in negatively charged state and a structure configuration that contains a Cu_3 metal cluster with the same electrons added.

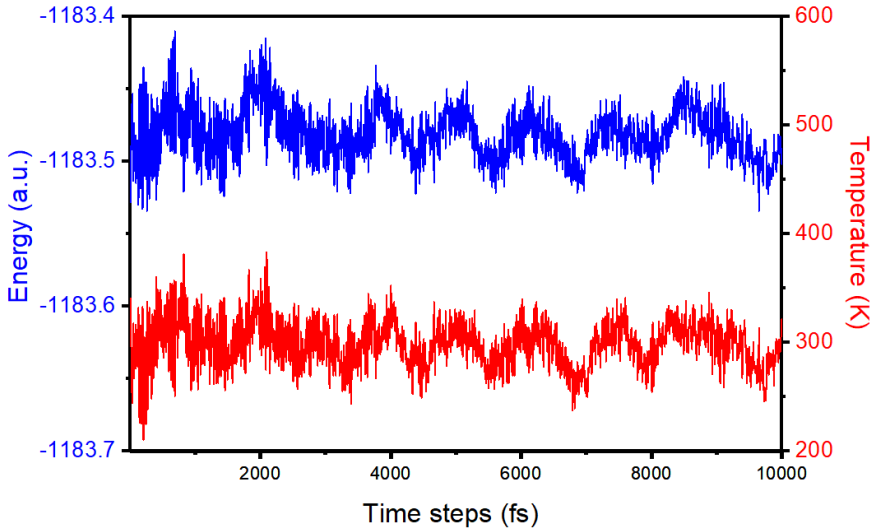

Figure S29. Variations of temperatures and energies along with time steps for AIMD simulations of {Cu_8}, the simulation is performed at 300 K for 5 ps with a time step of 0.5 fs.

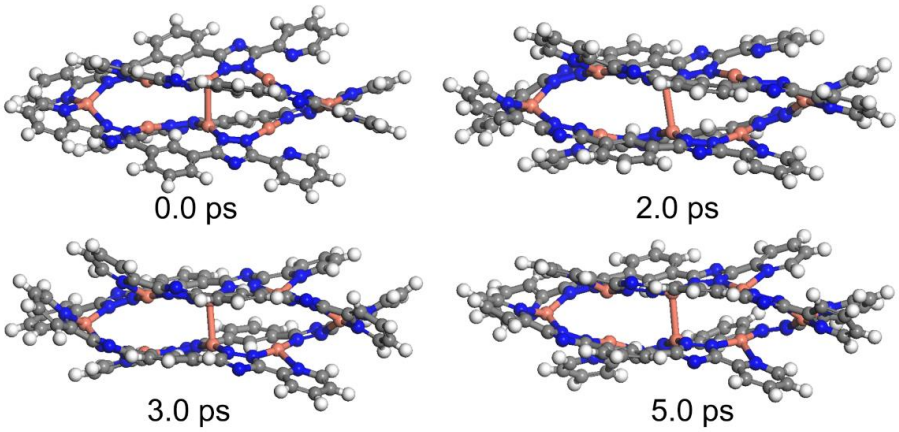

Figure S30. Snapshots from AIMD simulations of {Cu_8} of 0.0 ps, 2.0 ps, 3.0 ps, and 5.0 ps respectively.

The high stability of the Cu(I) sites is attributed to the strong binding between Cu atoms and surrounding N atoms and cuprophilic interaction from the opposite Cu(I) ions, even when the Cu(I) are reduced to intermediate state of Cu(x) ($0 \leq x < 1$). To prove this, we performed further energy calculations and *ab-initio* molecule dynamic (AIMD) simulations considering the applied potentials. For a charged {Cu_8} fragment, the charge density difference between a neutral state and a charged state (Figure S27) shows that added electrons are mainly located on the top Cu sites, which can be considered as reduced Cu sites. We then compare the relative energies between the {Cu_8} fragment in negatively charged state and a structure configuration that contains a Cu_3 metal cluster (in the same negatively charged state) as illustrated in Figure S28. In terms of thermodynamics, the formation of Cu clusters in metallic state is unfavorable by more than 2 eV, suggesting the formation of Cu clusters is rather difficult under negative potential. To link the added charges with the applied potentials in experiments, periodic calculations are further performed to obtain the work function of the system, then the applied potential is calculated with respect to the normal hydrogen electrode (details see computational methods). The results indicate that the applied potential can reach to ~2.0 V when one electron is added to the system. Therefore, the electroreduction condition can be simulated based on the charged system. Next, the stability of the electrocatalysts is further evaluated by using AIMD simulations at 300 K for 5 ps with a time step of 0.5 fs and two extra electrons. It can be found that both temperature and energy for the charged system are oscillating around the equilibrium state (Figure 29). More importantly, the whole framework of the system is well maintained during the AIMD simulations and no clustering of Cu sites is observed, indicating the high stability of the electrocatalytic system (Figure 30 and Movie S1).

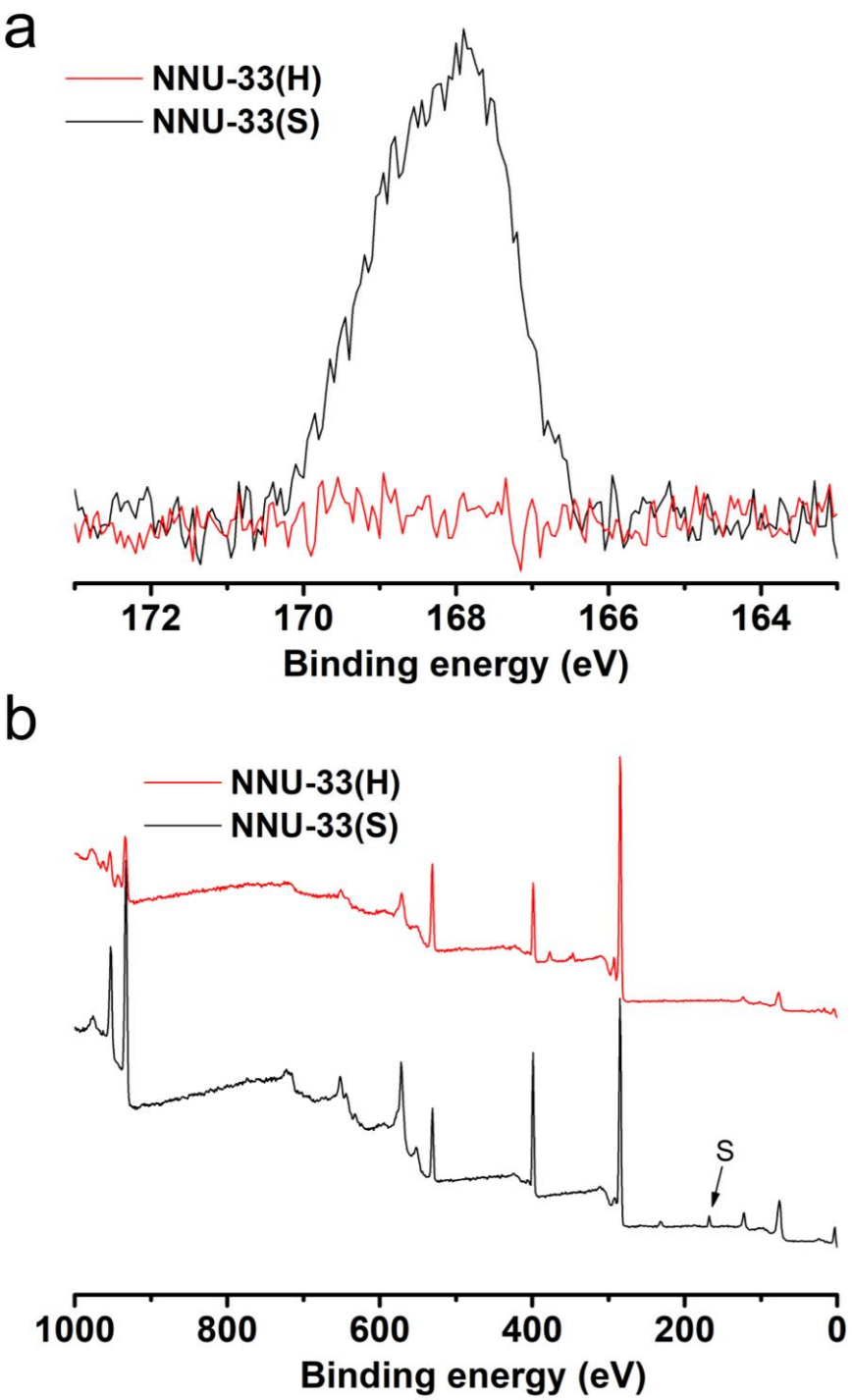

Figure S31. a XPS patterns for **NNU-33(S)** and **NNU-33(H)**. **b** the change of S 2p peaks in the XPS spectra of **NNU-33** and **NNU-33(H)**.

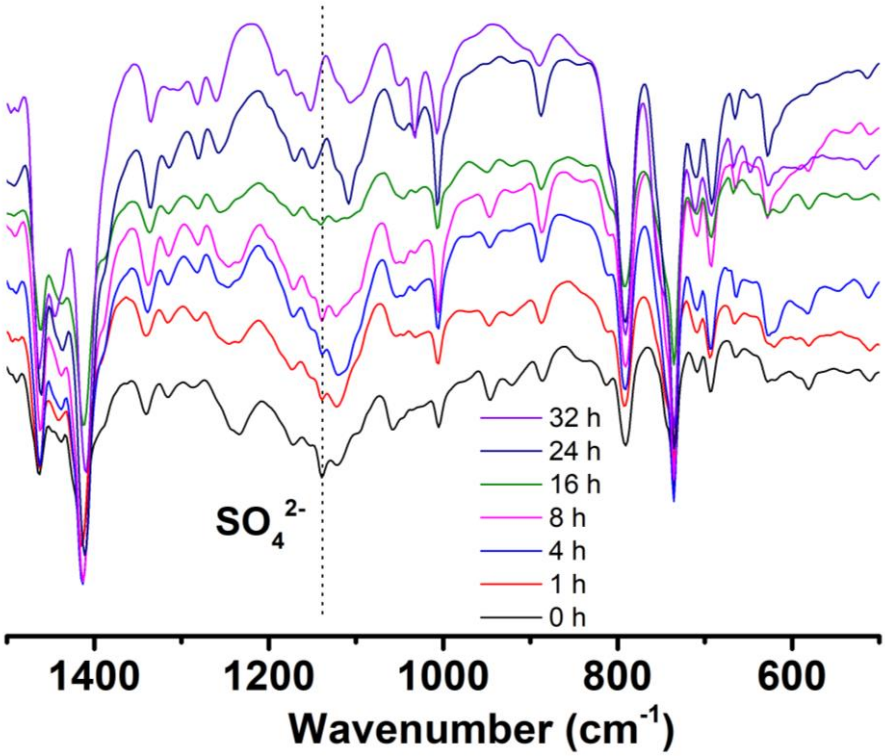

Figure S32. FTIR curves for **NNU-33(S)** after immersion in alkaline solution (1 M KOH) for different times. It can be found that, with increase the time for **NNU-33(S)** soaking in 1 M KOH, the peaking corresponding to SO_4^{2-} gradually disappeared, which suggested that SO_4^{2-} was replaced by OH^-.

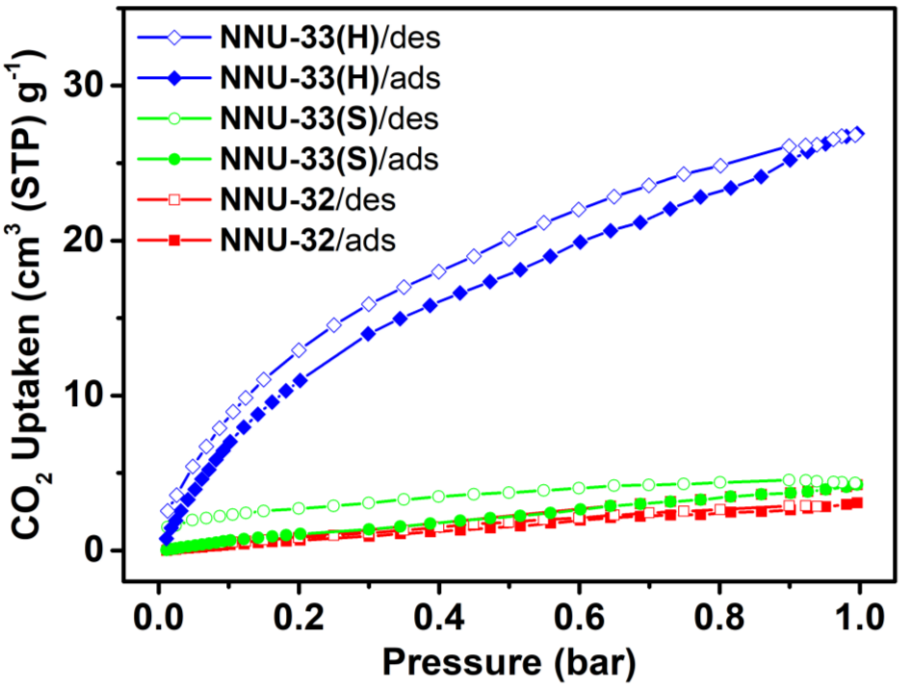

Figure S33. The CO_2 adsorption isotherms at 298 K of **NNU-32**, **NNU-33(S)** and **NNU-33(H)**.

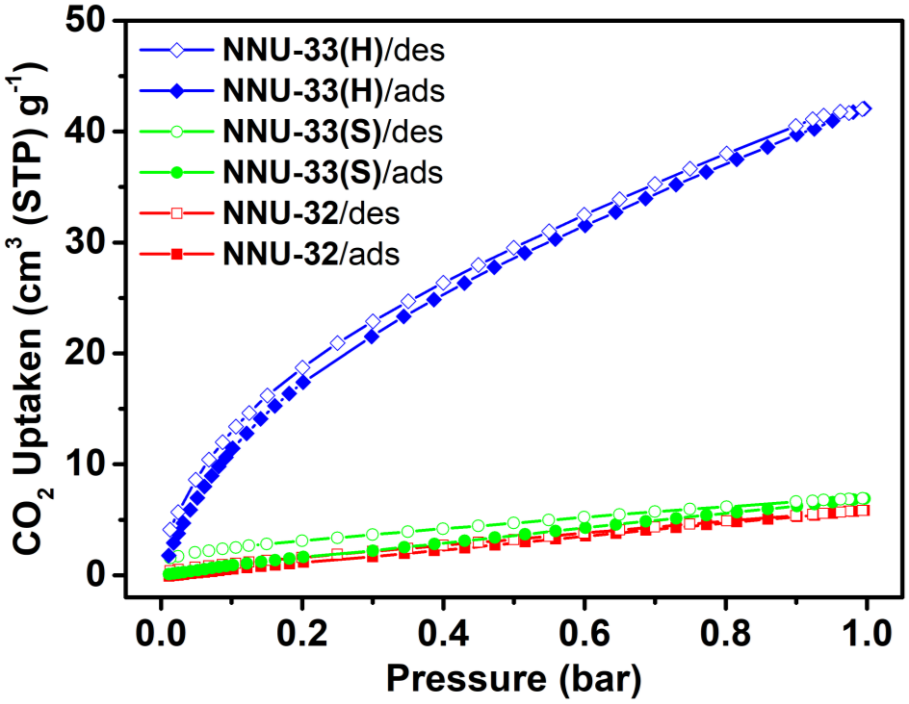

Figure S34. The CO_2 adsorption isotherms at 273 K of **NNU-32**, **NNU-33(S)** and **NNU-33(H)**.

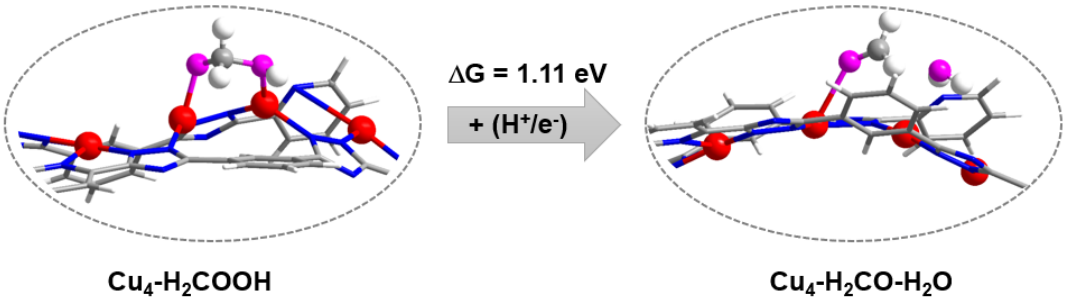

Figure S35. The free energy of PDS process (*H_2COOH → *OCH_2) calculated by taking half of the model into account.

Reference

1. Sheldrick, G. SHELXT - Integrated space-group and crystal-structure determination. *Acta Crystallogr. Sect. A*. **2015**, 71, 3-8.
2. Sheldrick, G. Crystal structure refinement with SHELXL. *Acta Crystallogr. Sect. C.* **2015**, 71, 3-8.
3. Dolomanov, O. V.; Bourhis, L. J.; Gildea, R. J.; Howard, J. A. K.; Puschmann, H. OLEX2: a complete structure solution, refinement and analysis program. *J. Appl. Crystallogr*. **2009**, 42, 339-341.
4. Alexandrov, E. V.; Blatov, V. A.; Kochetkov, A. V.; Proserpio, D. M. Underlying nets in three-periodic coordination polymers: topology, taxonomy and prediction from a computer-aided analysis of the Cambridge Structural Database. *CrystEngComm*. **2011**, 13, 3947-3958.
5. Frisch, M. J.; Trucks, G. W.; Schlegel, H. B.; Scuseria, G. E.; Robb, M. A.; Cheeseman, J. R.; Scalmani, G.; Barone, V.; Mennucci, B.; Petersson, G. A.; Nakatsuji, H.; Caricato, M.; Li, X.; Hratchian, H. P.; Izmaylov, A. F.; Bloino, J.; Zheng, G.; Sonnenberg, J. L.; Hada, M.; Ehara, M.; Toyota, K.; Fukuda, R.; Hasegawa, J.; Ishida, M.; Nakajima, T.; Honda, Y.; Kitao, O.; Nakai, H.; Vreven, T.; Montgomery, J. A.; Peralta, Jr. J. E.; Ogliaro, F.; Bearpark, M.; Heyd, J. J.; Brothers, E.; Kudin, K. N.; Staroverov, V. N.; Kobayashi, R.; Normand, J.; Raghavachari, K.; Rendell, A.; Burant, J. C.; Iyengar, S. S.; Tomasi, J.; Cossi, M.; Rega, N.; Millam, J. M.; Klene, M.; Knox, J. E.; Cross, J. B.; Bakken, V.; Adamo, C.; Jaramillo, J.; Gomperts, R.; Stratmann, R. E.; Yazyev, O.; Austin, A. J.; Cammi, R.; Pomelli, C.; Ochterski, J. W.; Martin, R. L.; Morokuma, K.; Zakrzewski, V. G.; Voth, G. A.; Salvador, P.; Dannenberg, J. J.; Dapprich, S.; Daniels, A. D.; Farkas, O.; Foresman, J. B.; Ortiz, J. V.; Cioslowski, J.; Fox, D. J.. Gaussian 09, Revision D.01 (Gaussian Inc.; Wallingford, CT, 2013).
6. Zhao, Y.; Truhlar, D. G. The M06 suite of density functionals for main group thermochemistry, thermochemical kinetics, noncovalent interactions, excited states, and transition elements: two new functionals and systematic testing of four M06-class functionals and 12 other functionals. *Theor. Chem. Acc*. **2008**, 120, 215-241.
7. Hay, P. J.; Wadt, W. R. Ab initio effective core potentials for molecular calculations—potentials for K to Au including the outermost core orbitals. *J. Chem. Phys.* **1985**, 82, 299-310.
8. Pople, J. A.; Hehre, W. J.; Pople, J. A. Self-consistent molecular-orbital methods. IX. An extended Gaussian-type basis for molecular-orbital studies of organic molecules. J. *Chem. Phys*. **1971**, 54, 724-728.
9. Tomasi, J.; Mennucci, B.; Cammi, R. Quantum mechanical continuum solvation models. *Chem. Rev.* **2005**, 105, 2999-3094.
10. Bader, R. F. W. Atoms in molecules –A Quantum Theory, Oxford Unvieristy Press Oxford (1990).
11. Lu,T.; Chen, F. Multiwfn: A multifunctional wavefunction analyzer. *J. Comput. Chem*. **2012**, 33, 580-592.
12. Benard, M.; Coppens, P.; DeLucia, M. L.; Stevens, E. D. Experimental and

theoretical electron density analysis of metal-metal bonding in dichromiumtetraacetate. *Inorg. Chem*. **1980**, 19,1924-1930.
13. Jenkins, S.; Morrison, I. The chemical character of the intermolecular bonds of seven phases of ice as revealed by ab initio calculation of electron densities. *Chem. Phys. Lett.* **2000**, 317, 97-102.
14. Espinosa, E.; Alkorta, I.; Elguero, J.; Molins, E. From weak to strong interactions: A comprehensive analysis of the topological and energetic properties of the electron density distribution involving X–H···F–Y systems. *J. Chem. Phys*. **2002**, 117, 5529-5542.
15. Varadwaj, P. R.; Marques, H. M. The physical chemistry of coordinated aqua-, ammine-, and mixed-ligand Co^{2+} complexes: DFT studies on the structure, energetics, and topological properties of the electron density. *Phys. Chem. Chem. Phys*. **2010**, 12, 2126-2138.
16. Cremer, D.; Kraka, E. Chemical bonds without bonding electron density — does the difference electron-density analysis suffice for a description of the chemical bond? *Angew. Chem. Int.* **1984**, 23, 627-628.
17. Nørskov, J. K.; Rossmeisl, J.; Logadottir, A.; Lindqvist, L.; Kitchin, J. R.; Bligaard, T.; Jónsson, H. Origin of the overpotential for oxygen reduction at a Fuel-Cell cathode. *J. Phys. Chem. B*. **2004**, 108, 17886-17892.
18. Kresse, G.; Hafner, J. *Ab initio* molecular dynamics for open-shell transition metals. *Phys. Rev. B.* **1993,** 48, 13115-13118.
19. Kresse, G.; Furthmüller, J. Efficient iterative schemes for *ab initio* total-energy calculations using a plane-wave basis set. *Phys. Rev. B.* **1996,** 54, 11169-11186.
20. Kresse, G.; Furthmüller, J. Efficiency of ab-initio total energy calculations for metals and semiconductors using a plane-wave basis set. *Comput. Mater. Sci.* **1996,** 6, 15-50.
21 Perdew, J. P.; Burke, K.; Ernzerhof, M. Generalized Gradient Approximation Made Simple. *Phys. Rev. Lett.* **1996,** 77, 3865-3868.
22. Blöchl, P. E. Projector augmented-wave method. *Phys. Rev. B.* **1994,** 50, 17953-17979.
23. Mathew, K.; Kolluru, V. S. C.; Mula, S.; Steinmann, S. N.; Hennig, R. G. Implicit self-consistent electrolyte model in plane-wave density-functional theory. *J. Chem. Phys.* **2019,** 151, 234101.
24. Mathew, K.; Sundararaman, R.; Letchworth-Weaver, K.; Arias, T. A.; Hennig, R. G. Implicit solvation model for density-functional study of nanocrystal surfaces and reaction pathways. *J. Chem. Phys.* **2014,** 140, 084106.
25. *CP2K developers group under the terms of theGNUGeneral Public Licence 2015 see www.cp2k.org*.
26. VandeVondele, J.; Krack, M.; Mohamed, F.; Parrinello, M.; Chassaing, T.; Hutter, J., *Comput.* Quickstep: Fast and accurate density functional calculations using a mixed Gaussian and plane waves approach. *Phys. Commun.* **2005,** 167, 103-128.
27. VandeVondele, J.; Hutter, J. Gaussian basis sets for accurate calculations on molecular systems in gas and condensed phases. *J. Chem. Phys.* **2007,** 127, 114105.
28. Goedecker, S.; Teter, M.; Hutter, J. Separable dual-space Gaussian

pseudopotentials. *Phys. Rev. B.* **1996,** 54, 1703-1710.
29. Grimme, S.; Antony, J.; Ehrlich, S.; Krieg, H. A consistent and accurate ab initio parametrization of density functional dispersion correction (DFT-D) for the 94 elements H-Pu. *J. Chem. Phys.* **2010,** 132, 154104.
30. Andreussi, O.; Dabo, I.; Marzari, N. Revised self-consistent continuum solvation in electronic-structure calculations. *J. Chem. Phys.* **2012,** 136, 064102.
31. Fattebert, J.-L.; Gygi, F. Density functional theory for efficient ab initio molecular dynamics simulations in solution. *J. Comput. Chem.* **2002,** 23, 662-666.
32. Yin, W.-J.; Krack, M.; Li, X.; Chen, L.-Z.; Liu, L.-M. Periodic continuum solvation model integrated with first-principles calculations for solid surfaces. *Prog. Nat. Sci.* **2017,** 27, 283-288.
33. Li, Q.; Zhao, Y.; Guo, J.; Zhou, Q.; Chen, Q.; Wang, J. On-surface synthesis: a promising strategy toward the encapsulation of air unstable ultra-thin 2D materials. *Nanoscale.* **2018,** 10, 3799-3804.
34. Chen, S.; Su, Y.; Deng, P.; Qi, R.; Zhu, J.; Chen, J.; Wang, Z.; Zhou, L.; Guo, X.; Xia, B.-Y. Highly Selective Carbon Dioxide Electroreduction on Structure-Evolved Copper Perovskite Oxide toward Methane Production. *ACS Catal*. **2020**, 10, 4640-4646.
35. Gregorio, G. L. D.; Burdyny, T.; Loiudice, A.; Lyengar, P.; Smith, W. A.; Buonsanti, R. Facet-Dependent Selectivity of Cu Catalysts in Electrochemical CO_2 Reduction at Commercially Viable Current Densities. *ACS Catal*. **2020**, 10, 4854-4862.
36. Qiu, Y-L.; Zhong, H-X.; Zhang, T-T.; Xu, X-F.; Zhang, H-M. Copper Electrode Fabricated via Pulse Electrodeposition: Toward High Methane Selectivity and Activity for CO2 Electroreduction. *ACS Catal*. **2017**, 7, 6302-6310.
37. Hu, Q.; Wang, X.; Li, G.; Wang, Z.; Huang, X.; Yang, H.; Ren, X.; Zhang, Q.; Liu, J.; He, C. Facile Synthesis of Sub-Nanometric Copper Clusters by Double Confinement Enables Selective Reduction of Carbon Dioxide to Methane. *Angew. Chem. Int. Ed*. **2020**, 59, 19054-19059.
38. Manthiram, K.; Beberwyck, B. J.; Alivisatos, A. P. Enhanced Electrochemical Methanation of Carbon Dioxide with a Dispersible Nanoscale Copper Catalyst. *J. Am. Chem. Soc*. **2014**, 136, 13319-13325.
39. Weng, Z.; Wu, Y.; Wang, M.; Jiang, J.; Yang, K.; Huo, S.; Wang, X.-F.; Ma, Q.; Brudvig, G. W.; Batista, V. S.; Liang, Y.; Feng, Z.; Wang, H. Active sites of copper-complex catalytic materials for electrochemical carbon dioxide reduction. *Nat. Commun*. **2018**, 9, 415.
40. Tan, X.; Yu, C.; Zhao, C.; Huang, H.; Yao, X.; Han, X.; Guo, W.; Cui, S.; Huang, H.; Qiu, J. Restructuring of Cu_2O to Cu_2O@Cu-Metal−Organic Frameworks for Selective Electrochemical Reduc-tion of CO_2. *ACS Appl. Mater. Interfaces.* **2019**, 11, 9904-9910.
41. Wang, Y.; Chen, Z.; Han, P.; Du, Y.; Gu, Z.; Xu, X.; Zheng, G. Single-Atomic Cu with Multiple Oxygen Vacancies on Ceria for Electrocatalytic CO_2 Reduction to CH4. *ACS Catal.* **2018**, 8, 7113-7119.

42. Varela, A. S.; Ju, W.; Reier, T.; Strasser, P. Tuning the Catalytic Activity and Selectivity of Cu for CO_2 Electroreduction in the Presence of Halides. *ACS Catal*. **2016**, 6, 2136-2144.
43. Li, Y.; Cui, F.; Ross, M. B.; Kim, D.; Sun, Y.; Yang, P. Structure-Sensitive CO_2 Electroreduction to Hydrocarbons on Ultrathin 5-fold Twinned Copper Nanowires. *Nano Lett*. **2017**, 17, 1312-1317.